Chronic Glucocorticoid Stress Reveals Increased Energy Expenditure and Accelerated Aging as Cellular Features of Allostatic Load

Natalia Bobba-Alves[1], Gabriel Sturm[1], Jue Lin[2], Sarah A Ware[3], Kalpita R. Karan[1], Anna Monzel[1], Céline Bris[4,5], Vincent Procaccio[4,5], Guy Lenaers[4,5], Albert Higgins-Chen[6], Morgan Levine[7], Steve Horvath[8], Balaji S Santhanam[9], Brett A Kaufman[3], Michio Hirano[10], Elissa Epel[11], Martin Picard[1,10,12]*

[1] Department of Psychiatry, Division of Behavioral Medicine, Columbia University Irving Medical Center, New York NY, United States

[2] Department of Biochemistry and Biophysics, University of California San Francisco, San Francisco CA, United States

[3] Department of Medicine, Vascular Medicine Institute and Center for Metabolic and Mitochondrial Medicine, University of Pittsburgh, Pittsburgh PA, United States

[4] Département de Biochimie et Génétique, CHU d'Angers, Angers, France

[5] MitoLab, UMR CNRS 6015, INSERM U1083, Institut MitoVasc, Université d'Angers, Angers, France

[6] Department of Psychiatry, Yale University School of Medicine, New Haven CT, United States

[7] Department of Pathology, Yale University School of Medicine, New Haven, CT, United States

[8] Department of Human Genetics, David Geffen School of Medicine, University of California Los Angeles, Los Angeles CA, United States

[9] Departments of Biological Sciences, Systems Biology, and Biochemistry and Molecular Biophysics, Institute for Cancer Dynamics, Columbia University, New York, United States

[10] Department of Neurology, Merritt Center, Columbia Translational Neuroscience Initiative, Columbia University Irving Medical Center, New York NY

[11] Department of Psychiatry and Behavioral Sciences, University of California San Francisco, San Francisco CA, United States

[12] New York State Psychiatric Institute, New York NY

* Correspondence: martin.picard@columbia.edu

Abstract

Stress triggers energy-dependent, anticipatory responses that promote survival, a phenomenon termed allostasis. However, the chronic activation of allostatic responses results in allostatic load (AL) and in the maladaptive state known as allostatic overload. Epidemiological studies show that allostatic load predicts physical and cognitive decline, as well as earlier mortality; yet the manifestations of allostatic load and overload at the cellular level remain unclear. To define the energetic cost and potential detrimental effects of prolonged cellular allostatic load, we developed a longitudinal model of chronic glucocorticoid stress in primary human fibroblasts. Results replicated in three healthy donors demonstrated that chronic stress robustly increased cellular basal energy consumption by 62%. This hypermetabolic state relied on a bioenergetic shift away from glycolysis towards mitochondrial oxidative phosphorylation (OxPhos), supported by an upregulation of mitochondrial biogenesis and increased mitochondrial DNA (mtDNA) density. As in humans where chronic stress accelerates biological aging, chronic allostatic load altered extracellular cytokine and cell-free DNA, caused mtDNA instability, increased the rate of epigenetic aging based on DNA methylation clocks, accelerated telomere shortening, and reduced lifespan (i.e., Hayflick limit). Pharmacological blockade of mitochondrial nutrients uptake normalized OxPhos activity but exacerbated hypermetabolism, which further accelerated telomere shortening and reduced cellular lifespan. Together, these results highlight the increased energetic cost of cellular allostatic load and suggests a mechanism for the transduction of chronic stress into accelerated cellular aging to be examined in humans.

Keywords: glucocorticoid, chronic stress, mitochondria, allostatic load, allostatic overload, aging, hypermetabolism, telomere, epigenetic aging

Introduction

In response to environmental factors and stressors, living organisms mount evolutionarily conserved responses that aim to increase resilience and promote survival, a phenomenon termed *allostasis*[1,2]. However, the chronic activation of these allostatic responses produce *allostatic load*[3,4], reflecting the added cost of stress on the organism. When chronically activated, allostatic load can result in the maladaptive state of *allostatic overload*, which disrupt normal physiological functions and longevity[7]. For example, while regular exercise improves glucose regulation and increases overall fitness[5], excessive or chronic exercise disrupts glucose homeostasis and insulin secretion[6]. Large-scale epidemiological studies also show that allostatic load, reflected by the co-elevation of stress hormones, metabolites, and cardiovascular risk parameters, predicts physical and cognitive decline, as well as earlier mortality[8,9], underscoring the long-term damaging effects that chronic activation of stress pathways has on human health. However, how allostatic load and overload manifests at the cellular level has not been fully defined.

Allostatic load involves anticipatory processes that prepare the organism for potential threats, but it comes at a cost. All allostatic processes must consume energy – gene expression and protein synthesis, enzymatic reactions, as well as hormone biosynthesis and secretion, all consume ATP[10]. In human cells, ATP is produced with moderate efficiency by glycolysis ($J_{\text{ATP-Glyc}}$) in the cytoplasm, and with highest efficiency by oxidative phosphorylation (OxPhos, $J_{\text{ATP-OxPhos}}$) within mitochondria. Intracellularly, maintaining glycolysis and OxPhos pathways come at a cost, which is substantially higher for OxPhos, owing to the extensive proteome cost of mitochondrial biogenesis and maintenance (>1,000 proteins) relative to glycolysis (~10 proteins)[11]. In addition to their role as the main energy producers, mitochondria respond to stress mediators[12] and influence physiological processes that encompass allostasis[13], positioning mitochondria as key mediators of cellular and whole-body stress responses[14]. We have previously outlined theoretical functional and structural mitochondrial recalibrations and potential detrimental effects that may occur in response to chronic stress, known as mitochondrial allostatic load (MAL)[15]. However, these hypothesized recalibrations, in particular the total energetic cost of allostatic load and the potential downstream maladaptive consequences, have not been defined longitudinally in a human system.

A major evolutionary-conserved stress pathway in mammals involves the release of glucocorticoids (GC; cortisol in humans, corticosterone in rodents). GC signaling acts via the glucocorticoid receptor influencing the expression of both nuclear[16] and mitochondrial genomes[17]. GC signaling in human fibroblasts also has been shown to acutely induce mitochondrial DNA (mtDNA) release into the cytoplasm[18]. In humans, chronic elevation of GC levels is linked to brain atrophy[19], cognitive decline and increased risk of Alzheimer disease[20,21], as well as increased risk of metabolic disease[20]. Therefore, based on previous short-term GC stimulation studies[12] and the fact that *any* allostatic process requires active, ATP-dependent molecular events (e.g., transcription and translation, protein secretion, organelle turnover, DNA replication and repair, epigenetic remodeling, etc.), we hypothesized that chronic GC signaling would trigger energy-dependent recalibrations among multiple domains of bioenergetic and cellular behavior. Moreover, based on evidence in humans that chronic allostatic load leads to allostatic overload manifesting as accelerated cellular aging[22,23] and increased risk of age-related diseases[24], we further hypothesized that that prolonged stress exposure in cells would trigger maladaptive outcomes among multiple cellular aging markers and lifespan.

Here we use a cellular system shown to recapitulate human epigenetic aging signatures *in vitro*[25] and enable to longitudinally examine several key hallmarks of human aging, including mitochondrial bioenergetics, secreted cytokines, epigenetic clocks, and markers of replicative senescence such as telomere length and the Hayflick limit[26]. To examine the bioenergetic and cellular manifestations of allostatic load across the lifespan, we apply chronic GC stimulation to three cell lines derived from three healthy donors, and deploy a longitudinal, high-frequency, repeated-measures approach. This model presents the major advantages of reducing potential bias from single-time points and to resolve some potential time-dependent effects of chronic GC stress. Together, our findings define the chronic effects of GC stress on cellular, bioenergetic and molecular recalibrations, highlighting increased energy expenditure (i.e., *hypermetabolism*) and accelerated cellular aging as interrelated, cell-autonomous features allostatic load.

Results

Chronic GC stress decreases cell volume and increases cell death

We treated human fibroblasts derived from three healthy donors (Donors 1, 2 and 3) with the GC receptor agonist dexamethasone (Dex, 100 nM), at a concentration that triggers its translocation from the cytoplasm to the nucleus in this cell type[18]. To evaluate the effects of chronic GC signaling across the cellular lifespan (up to 150-250 days, depending on the cell line), cytologic parameters where evaluated every 5-7 days, while cellular bioenergetics, secreted factors, DNA- and RNA-based measurements to quantify allostatic load were performed every 10-20 days until cells reached replicative senescence, marked by a near absence of cell division (**Fig. 1A**). A portion of lifespan data for the control (untreated) group was reported in [27], and here data from Dex-treated cell lines is expressed relative to their respective untreated control condition. Compared to similar experiments in an immortalized cell line(s), primary human fibroblasts derived from different female and male donors provide a more direct test of robustness and generalizability for our conclusions.

Chronic Dex altered cell morphology, marked by a flattened appearance with more membrane protrusions and fewer contacts with surrounding cells (**Fig. 1B**). Acutely (within 5 days), Dex caused a 25-50% reduction in cell volume that persisted across most of the cellular lifespan in all three donors, resulting in an average 33% volume reduction across the lifespan ($p<0.0001$, **Fig. 1D**). Towards the end of the lifespan between 200-250 days, both Dex-treated cells and controls converged towards the same apparent minimal cell volume. Parallel measures of cell death or mortality showed no acute effect of Dex on cell death for the first ~50 days. But Dex caused a marked elevation in cell death in the latter portion of the lifespan, reaching up to an order of magnitude increase for donor 3, and an average 3.3-fold increase across all three donors ($p<0.0001$, **Fig. 1E-F**). Thus, GC stress in our primary human cell system triggered robust time-dependent allostatic effects including a reduction in cell volume and an earlier rise of cell death, which suggested that chronically stressed cells may be under energetic constraints that limit survival and growth[28-32].

Chronic GC stress triggers hypermetabolism

Cellular energetic constraints could arise in two main ways: an increase in ATP consumption rate (i.e., energy expenditure), or a reduction in the capacity to produce ATP. To evaluate the effects of chronic Dex on total energy expenditure and ATP production capacity, we performed extracellular flux analysis of oxygen and pH (Seahorse) longitudinally, every 10-28 days (**Extended Data Fig. 1A**). Using a validated approach to converted oxygen consumption rate (OCR) and extracellular acidification rates (ECAR) to ATP production rates[33], we generated lifespan trajectories of three main parameters: i) resting (or basal) ATP production rates derived from glycolysis ($J_{\text{ATP-Glyc}}$) and from OxPhos ($J_{\text{ATP-OxPhos}}$), which reflects how much energy cells *consume* to sustain life and divide; ii) the maximal $J_{\text{ATP-Glyc}}$ detected after pharmacologically inhibiting OxPhos, which reflects the glycolytic capacity to fulfill basal cellular energetic demands; and iii) the maximal $J_{\text{ATP-OxPhos}}$, which reflects the built-in spare OxPhos capacity (**Extended Data Fig. 1B-C**). To obtain energy consumption per unit of cell mass (similar to measuring whole-body energy consumption per Kg of body weight in humans), bioenergetic measures were normalized to the closest available measurement in our model, cell volume.

Around day 25, Dex caused an initial decrease in $J_{\text{ATP-Glyc}}$, which subsequently oscillated but remained on average 16% lower than control across the lifespan ($p<0.05$, **Fig 2A**). In contrast, Dex substantially increased mitochondrially-derived $J_{\text{ATP-OxPhos}}$, which remained markedly elevated reaching up to 3-4-fold higher rates than control in mid-life ($p<0.0001$, **Fig 2B**). Absolute $J_{\text{ATP-Glyc}}$ and $J_{\text{ATP-OxPhos}}$ values showed similar longitudinal behaviors, with lifespan averages significantly lower and higher than controls, respectively ($ps<0.0001$, **Extended Data Fig. 2A-B).**

To gain insight into the total energetic costs of allostatic load, we then combined ATP production rates derived from both glycolysis and OxPhos. This showed that Dex increased total resting energy consumption across the lifespan ($J_{\text{ATP-Total}}$/cell volume) by a striking 61.9% ($p<0.001$, **Fig 2C**). Dex-treated cells consume more energy per unit of volume to sustain life. This chronic state of hypermetabolism suggested the existence of costly allostatic recalibrations that may also involve qualitative cellular bioenergetic recalibrations.

Chronic GC stress causes a metabolic shift towards OxPhos

Expressing $J_{\text{ATP-Glyc}}$ and $J_{\text{ATP-OxPhos}}$ as a percentage of $J_{\text{ATP-Total}}$ showed that that Dex induced a significant shift towards OxPhos as the major source of ATP. Across the lifespan, Dex-treated cells derived 75-80% of their ATP from OxPhos, compared to 55-60% in control cells ($p<0.0001$, **Fig 3A**). Accordingly, variations in $J_{\text{ATP-Total}}$ along the lifespan were mostly explained by $J_{\text{ATP-OxPhos}}$ ($r^2=0.87$, $p<0.0001$, **Extended Data Fig. 2D**), highlighting the strong reliance of total energy expenditure on mitochondrial OxPhos**.**

This result led us to examine whether chronic GC stress directly impaired glycolysis. By inhibiting OxPhos with the ATP synthase (i.e., Complex V) inhibitor oligomycin, normal cells naturally increase glycolytic activity to compensate for the missing $J_{\text{ATP-OxPhos}}$ and fulfill the cellular energetic demands. Here we found that after the addition of oligomycin, Dex-treated cells easily matched the basal $J_{\text{ATP-Total}}$ of their control counterparts by upregulating $J_{\text{ATP-Glyc}}$ (ns, **Fig. 3B**). The intact glycolytic capacity demonstrated that the metabolic shift towards OxPhos does not arise in response to impaired glycolysis, but potentially by actively upregulating the OxPhos system.

Accordingly, Dex increased the spare fraction of OxPhos capacity above basal consumption by an average of 83.9% ($p<0.0001$, **Fig. 3C**). Moreover, for a given amount of energy required to sustain basal cellular functions, Dex-treated fibroblasts maintained an even larger spare $J_{\text{ATP-OxPhos}}$ capacity than control cells – an effect that persisted across the lifespan ($p<0.0001$, **Fig. 3D**), consistent with the anticipatory process of allostasis.

To examine the basis for this amplified OxPhos capacity in cells experiencing allostatic load, we first evaluated mitochondrial coupling efficiency. Surprisingly, Dex did not alter coupling efficiency, which oscillated by no more than 10% (within measurement error) from the control across the lifespan (n.s., **Fig. 3E**), and therefore cannot explain neither the observed increased in the total energy expenditure, nor the elevated OxPhos spare capacity. We then quantified total cellular mitochondrial DNA copy number (mtDNAcn) by qPCR, which showed that Dex induced approximately a doubling in mtDNAcn over the first 100 days of lifespan, followed by more substantial elevation at the end of life, particularly in one of the donors. On average across the lifespan, Dex-treated cells had an average of

936 mtDNA copies per cell, 97.8% higher than the control group ($p<0.05$, **Extended Data Fig. 4**). Furthermore, when accounting for the observed reduction in cell volume, cellular mtDNA density was 152.8% higher than in control ($p<0.01$, **Fig. 3F**), consistent with the increased reliance on OxPhos, the higher spare respiratory capacity, and the overall hypermetabolism in chronically stressed cells.

Chronic GC stress upregulates OxPhos and mitochondrial biogenesis gene expression

To examine the transcriptional recalibrations associated with stress-induced cellular allostatic load and hypermetabolism, we performed RNA sequencing (RNAseq) at 9-10 timepoints across the lifespan of each donor, and systematically queried the major glycolytic enzymes as well as OxPhos and mtDNA-related genes. Consistent with the stable bioenergetic shift from glycolysis to OxPhos, chronic Dex downregulated most key glycolytic genes across the lifespan (**Fig. 4A**), including the first enzyme in the sequence from glucose to pyruvate, hexokinase (HK2, -44.4%, $p<0.001$), as well as the rate limiting enzyme phosphofructokinase (PFK, -28.5%, $p<0.001$). On the other hand, chronic Dex upregulated most individual subunits of the five OxPhos complexes. The most highly upregulated genes were UQCRC1 (complex III, +69.7%, $p<0.001$) and COX7A1 (complex IV, +52.2%, $p<0.01$), indicating a coordinated upregulation of the OxPhos program (**Fig. 4B**).

Moreover, consistent with the elevated mtDNAcn in Dex-treated cells, genes encoding mtDNA maintenance- and replication-related proteins were both upregulated **(Fig. 4C-D**). This included the DNA polymerase theta POLQ, which plays a key role on repairing double strand breaks by the theta-mediated end joining mechanism[34] (+91.9%, $p<0.001$). This result also pointed to potential mtDNA instability as a feature of MAL[15] (see below). Dex upregulated the master regulator of biogenesis PGC1α (peroxisome proliferator-activated receptor gamma coactivator 1-alpha, PPARGC1A[35]) by 106% across the lifespan ($p<0.001$, two-way ANOVA), and simultaneous downregulated the inhibitor of biogenesis NRIP1 (nuclear receptor interacting protein 1, also RIP140[36,37]) by 61.5% ($p<0.001$, two-way ANOVA) **(Fig. 4E**). Together, the transcriptomics data summarized in **Fig. 4F** (details in **Supplemental Data Fig. 1**) reveal a sustained stress-induced upregulation of the genetic programs involved in building additional OxPhos capacity and mtDNA copy number, consistent with the bioenergetic recalibrations and the anticipatory processes of cellular allostatic load in Dex-treated cells.

Chronic GC stress increases cell-free mtDNA levels

The changes in mitochondrial OxPhos and mtDNA density with allostatic load led us to investigate extracellular cell-free DNA (cf-mtDNA), an emerging mitochondria-derived signaling agent that can act as an inter-cellular signaling factor[38]. In humans, cf-mtDNA reflects the extracellular release of whole mitochondria or mitochondria-free mtDNA[39,40]. Elevated cf-mtDNA has been reported both in response to acute psychological stress[18,41] and with human aging[42]. In our system, chronic Dex strikingly increased media cf-mtDNA by 4-6-fold over the first 100 days in the three donors (**Fig. 5A**). Subsequently, cf-mtDNA levels appeared to oscillate and gradually match control levels. On average, cf-mtDNA levels across the lifespan were 46.9% higher in Dex-treated cells than controls ($p<0.05$). Consistent with evidence suggesting that cf-mtDNA release is a selective and regulated process not primarily driven by cell death (reviewed in [43,44]), cf-mtDNA was only moderately related to cell death at each passage. Cell death accounted for 22% and 43% of the variance in cf-mtDNA levels among control and Dex-treated cells, respectively (**Fig. 5B**).

Dex also robustly elevated cell-free nuclear DNA (cf-nDNA, measured in parallel with cf-mtDNA), which reached values an order of magnitude higher than controls within the first 100 days of treatment. As for cf-mtDNA, this initial response was followed by a gradual normalization, resulting in a lifespan average 2-fold higher than controls ($p<0.001$, **Fig. 5C**). Similar to cf-mtDNA, cell death was significantly correlated with cf-nDNA but accounted for only a minor fraction (10-14%) of the variance in extracellular nuclear genome (**Fig. 5D**).

Interestingly, whereas media cf-mtDNA and cf-nDNA were strongly correlated in control cells ($r^2=0.64$, $p<0.0001$), in response to chronic Dex, a large number of cf-mtDNA molecules were released at certain timepoints (up to 10-fold) without a corresponding elevation in cf-nDNA, as reflected in a markedly reduced correlation between cf-mtDNA and cf-nDNA ($r^2=0.13$, $p<0.05$, **Extended Data Fig. 4A**). This result largely, although not definitively, ruled out the possibility that both genomes are systematically co-released during glucocorticoid stress. Moreover, the extracellular mitochondrial-to-nuclear ratio (cf-mtDNA/cf-nDNA) in the extracellular space was not correlated with intracellular mtDNA/nDNA ratio (mtDNAcn), supporting the notion that the underlying release mechanisms between the mitochondrial and nuclear genomes are different (**Extended Data Fig. 4B-D)**. These data define the temporally sensitive release of extracellular genomic material as a feature of GC-induced cellular allostatic load.

Chronic GC stress alters cytokine release

Given the observed increase in extracellular cf-DNA, and considering that allostatic load in humans is characterized by elevated levels of neuroendocrine mediators[45,46] as well as chronic inflammation[47], we next sought to investigate the effects of chronic Dex on the profiles of secreted cytokines. Using a custom-designed Luminex array of plasma cytokines associated with human aging[48], we detected a panel of 27 cytokines in the culture media of the three donors across the lifespan (**Fig. 6A**). While chronic Dex caused variable responses among different cytokines, it triggered a pattern of acute increase in many cytokine levels within the first 60 days of treatment, consistent with the classic inverted-U shaped response of allostasis[12] (**Fig 6B**). The peak cytokine response occurred around ~30 days after the onset of stress, with a magnitude approximately double (i.e., ~100% increase) for most cytokines relative to control cells.

Further analysis revealed that Dex significantly altered the lifespan average secretion of 12 out of the 27 age-related cytokines. The strongest response was a stable elevation (average +210%) of Tissue Factor Pathway Inhibitor (TFPI, $p<0.001$, **Fig. 6C**), a cytokine related to the complement and coagulation cascades. The most strongly downregulated cytokine was Interleukin 6 (IL6, -77%, $p<0.001$, **Fig. 6D**), a pro-inflammatory cytokine well-known to be repressed by GC signaling[49].

Interestingly, when we queried the same cytokines at the transcript level, we observed a global downregulation in RNA levels among the three donors (**Extended Data Fig. 5A-B**). In addition, the effect sizes across the lifespan were 2-3 times larger at the RNA level than at the extracellular protein level (**Extended Data Fig. 5C-D**). Comparison of the secreted protein and transcriptomic data demonstrated that only half of the cytokines showed congruent (within 10% variation) responses, highlighting a disconnect between quantitative measures of gene expression and cytokine release, and emphasizing the value of direct protein quantification (**Supplemental Data Fig. 2A-AB**). Thus, chronic GC signaling triggers a time-sensitive secretory phenotype, possibly involving non-transcriptional and/or non-genomic effects in the release of age-related cytokines.

Chronic GC stress causes mtDNA instability

Thus far, we have examined key bioenergetic features of cellular allostatic load and related extracellular signaling behavior. We now turn our attention to potential maladaptive consequences of sustained allostatic load, namely evidence of mitochondrial and cellular allostatic overload. *In vitro* and *in vivo* studies have shown that one of the consequences of chronic metabolic stressors, OxPhos defects, and aging is mtDNA instability, manifested as the accumulation of mtDNA defects[50-54]. We also recently demonstrated that mtDNA instability can be induced by OxPhos defects in this cellular lifespan system[27].

In Dex-treated cells, long-range PCR (LR-PCR) provided initial evidence that chronic glucocorticoid signaling may trigger mtDNA instability, as illustrated in multiple mtDNA deletions detected at different time points across the lifespan in two (Donors 1 and 2) out of three donors (Donor 1 shown in **Fig 7A**). We confirmed the accumulation of mtDNA deletions in all donors through deep mtDNA sequencing and quantified their relative abundance (i.e. proportion of mutant and normal mtDNA genomes, or heteroplasmy) across the lifespan using the eKLIPse pipeline[55] (**Fig 7B, Extended Data Fig 6A**). Dex induced a relatively large increase in total mtDNA deletion levels between days 20-50 of treatment among all three donors, suggesting that the effects of glucocorticoid stress on mtDNA in instability may develop relatively rapidly. These timepoints also correspond to the acute elevation in cytokines (between days 20-50, see Fig 6). On average, Dex tended to increase the total mtDNA deletion burden by an average of 141.1% (p=0.11, **Fig 7C**). This trend in mtDNA deletion load was not driven by an increase in the number of unique deletions, but rather by higher heteroplasmy levels of deletions that were i) moderately larger in size and ii) tended to affect the D-loop the sequence where the mtDNA maintenance proteins whose gene expression were upregulated (see Fig 4F) are known to physically interact (**Extended Data Fig 6B-E**).

Another marker of mtDNA instability is the accumulation of point mutations. Along the lifespan, except for one low heteroplasmy mutation in Donor 2 detected on day 125, control cells largely did not accumulate novel mutations. In comparison, during the same portion of lifespan we identified 3 and 4 novel mutations in Donors 1 and 2 (total 7 novel mutations), one of which clonally expanded to reach 39.8% heteroplasmy (**Figure 7D**).

Thus, as expected replicating cultured cells accumulate few novel mtDNA deletions and point mutations[56], likely as a result of purifying selection (fibroblasts with deleterious mtDNA defects die and are eliminated). Nevertheless, the apparent elevation in both spontaneous deletions and point mutations are consistent with the accumulation of mitochondrial allostatic load, and collectively point to mtDNA instability as a potential feature of GC-induced hypermetabolism and cellular allostatic load.

Chronic GC stress accelerates cellular aging

Combined, the mtDNA instability, premature cell size reduction, elevated mortality, as well as the early induction of most human age-related cytokines suggested that cellular allostatic load could impact aging trajectories. We first examine the growth curves for each donor, which reveal the maximal number of cell divisions (i.e., population doublings) that can be accomplished by each donor before reaching replicative senescence. This feature, also known as the Hayflick limit[57,58], is the most closely related outcome to human lifespan in this simple cellular model and could reflect allostatic overload.

Consistent with the notion that chronic stress accelerates cellular aging in humans (reviewed in [59,60]), Dex caused a premature halting of population doubling (**Fig. 8A**), resulting in an average 19.8% reduction in the Hayflick limit across the three donors (p<0.05, **Fig. 8B**). This effect was associated with a decrease in cell division rate within the first 50 days of treatment (-39.1%, p<0.05, **Fig. 8C, Extended Data Fig. 7**). In the context of this substantial reduction in the division rate, and particularly given the reduced cell size in Dex-treated cells (-25-50% volume), the hypermetabolic phenotype of allostatic load becomes particularly striking. Considering cellular doubling rate and cell size, chronically stressed fibroblasts expend 107.9% more energy than control cells over the course of *each cell division* (p<0.001, **Extended Data Fig. 7**).

To examine the potential basis for the reduced cellular lifespan, we next examined two orthogonal measures of replicative senescence and cellular aging: telomere length[22], and DNA methylation-based epigenetic clocks[61,62]. The following results must be interpreted in the context of the limited number of observations where which all lifespan timepoints are collapsed into a single slope/value (n=3 donors), such that the effect size (% change) is likely more meaningful than the p values. We first quantified relative telomere length by qPCR across the lifespan for each donor and computed the rate (i.e., linear slope) of telomere shortening per cell division. Chronic Dex accelerated the telomere shortening rate by 27.6% across the three donors ($p<0.05$, **Fig. 7D**). Telomere length was also estimated through a DNA methylation-based algorithm[63]. This measure documented a trend of similar magnitude towards accelerated shortening rate per population doubling (+39.4%, $p=0.11$, **Extended Data Fig. 8A-B**). These data thus provided converging evidence that chronically stressed cells experience more rapid loss of telomeric repeats during each event of genome replication, consistent with allostatic overload.

At the gene expression level, accelerated telomere attrition was associated with an alteration in the expression of genes encoding telomere capping proteins. In particular, the major component of the shelterin complex, TPP1[64] was significantly downregulated across the lifespan for the three donors (-26.7%, $p<0.0001$), potentially indicating that the telomeres in Dex-treated cells could be less extensively protected (**Extended Data Fig. 8C-D**). On the other hand, several genes encoding the core components of the telomerase holoenzyme[64] were upregulated, including TERC, which was the most highly upregulated telomerase gene (+68.6%, $p<0.0001$, **Extended Data Fig. 8C-D**). The upregulation of TERC in the context of accelerated telomere shortening in Dex-treated is in agreement with clinical associations of chronic life stress and upregulation of telomerase activity in leukocytes[65,66], possibly reflecting a (failed) attempt to reactivate telomerase to preserve or elongate telomeres, turning chronic allostatic load to overload.

Chronological age can also be predicted with high accuracy through DNA methylation-based algorithms, known as epigenetic clocks[67-71]. Here, we generated a longitudinal DNA methylation dataset using the EPIC array[26], and deployed an approach that increases DNAmAge accuracy using a principal components-adjustment of the classic epigenetic clocks[72]. Applied across the cellular lifespan, we can longitudinally quantify the rate of epigenetic aging relative to population doublings. The results for the PC-adjusted PhenoAge clock[71] is shown in **Fig. 8E** and four other clocks (Horvath pan tissue, Hannum, Skin & blood, Grim age) are shown in **Extended Data Fig. 9**. Consistent with the telomere data, results across these five different epigenetic clocks indicated that chronic GC stress tended to accelerate the rate of epigenetic aging by an average of 70.0% ($p=0.055$, **Fig. 8F**). Together, these telomere and DNA methylation data provided converging evidence across two modalities linking chronic metabolic recalibrations to aging biology in primary human cells experiencing allostatic overload.

Age-related hypermetabolism and cell death occur near-synchronously

Given the premature age-related rise in cell death (see Fig 1) and the profound mitochondrial and bioenergetic recalibrations associated with increased energy consumption (see Figs 2 and 3) in Dex-treated cells, we leveraged the longitudinal nature of our dataset to examine whether cell death was temporally related to hypermetabolism. Plotting both mortality (% cell death) and total energy expenditure (J_{ATPtotal}/cell volume) relative to population doublings demonstrated that chronic Dex caused a left shift in the mortality curves, towards an earlier onset along the lifespan (**Fig. 8G**, *upper* panels). Strikingly, Dex caused a similar and near synchronous left shift in energy expenditure trajectories, reflecting an early onset, hypermetabolic state that develops over weeks (**Fig. 8G**, *lower* panels). Comparing both mortality and energy expenditure at matched timepoints revealed a strong temporal association across the entire lifespan, among both control and Dex-treated cells (r^2=0.84 and r^2=0.75, respectively, ps<0.001, **Fig. 8H**), meaning that the majority of the variation in cell death can be explained by the basal energy expenditure (i.e., how much energy cells must consume to sustain allostatic load), and vice-versa. These results therefore underscore the close temporal association between the energetic cost of allostatic load (i.e., hypermetabolism) and possibly the ultimate consequence of allostatic overload, death or mortality.

Hypermetabolism, not the metabolic shift towards OxPhos, predicts cell death

Previous work suggested that the shift from glycolysis towards OxPhos (as in the differentiation of stem cells to “mortal” cell lineages) drives the susceptibility to detrimental age-related molecular alterations[73]. And mitochondria appear required for key features of senescence[74]. Therefore, we investigated whether in our model of cellular allostatic load the association of hypermetabolism with cell death and lifespan was specifically related to increased mitochondrial OxPhos activity ($J_{\mathrm{ATP\text{-}OxPhos}}$), or the total energy expenditure ($J_{\mathrm{ATP\text{-}Total}}$).

To disentangle these factors, we repeated the chronic Dex lifespan experiments while simultaneously downregulating OxPhos activity using a combination of inhibitors to block the mitochondrial import of the major carbon sources: pyruvate (UK5099[75]), fatty acids (Etomoxir[76]), glutamine (BPTES[77]) (**Fig 9A**, **Extended Data Fig. 10A**). As expected, the mitochondrial nutrient uptake inhibitors (mitoNUITs) decreased OxPhos-derived ATP production in Dex-treated cells by an average of 21.2% (p<0.0001, **Extended Data Fig. 10B)**. This partial inhibition of OxPhos was associated with a supra-compensatory increase in glycolytic ATP production rates (+443.2%, p<0.0001, **Extended Data Fig. 10C**). Consequently, the Dex+mitoNUITs treatment elevated $J_{\mathrm{ATP\text{-}Total}}$ above the energy demand in Dex-treated cells by an additional 78.9% (p<0.0001, **Fig. 9B**). Thus, compared to chronic Dex alone, Dex+mitoNUITs successfully suppressed OxPhos, and triggered an even more severe state of hypermetabolism sustained predominantly by glycolysis. Therefore, we reasoned that if the observed allostatic overload phenotype (accelerated aging and premature mortality) was driven by the enhanced energy flux through OxPhos, the addition of mitoNUITs should at least partially rescue it. On the other hand, if cellular allostatic overload was directly driven by the total energy expenditure and hypermetabolism, then Dex+mitoNUITs would aggravate the pro-aging effects of allostatic overload.

Consistent with the latter alternative, the Dex+mitoNUITs combination either exacerbated or did not alter the pro-aging effects of Dex. Compared to Dex alone, Dex+mitoNUITs reduced the Hayflick limit by a further 18.5% (n=3 donors, p<0.05, **Fig. 8D-F**). Accordingly, Dex+mitoNUITs tended to increased telomere erosion rate per population doubling by a similar proportion (+19.2%, p=0.45, **Fig. 8G**), although this did not reach statistical significance. However, the DNAm clocks-based rates of aging were not different between Dex and Dex+mitoNUITS (**Fig. 8H and 8I**), pointing to potential mechanistic divergences or to a ceiling effect for epigenetic clocks.

In relation to cell death, the Dex+mitoNUITs treatment combination left-shifted both the mortality and energy expenditure trajectories towards an earlier onset along the lifespan (**Fig 8J**), indicating a trend towards increased cell death (+28,6%, p=0.09). Again, the temporal association between energy expenditure and death across the lifespan remained strong and significant in Dex+mitoNUITs-treated cells (r^2=0.52, p<0.001). Thus, diverting energy flux from OxPhos and elevating hypermetabolism with Dex+mitoNUITs treatment further exacerbated allostatic overload and related age-related outcomes, implicating hypermetabolism, rather than flux through OxPhos, as the main driver of chronic stress-induced cellular allostatic overload.

Discussion

Although the long-term effects of chronic stress on organ systems (i.e. secondary effects) and clinical outcomes such as cognitive and functional decline leading to pathology (i.e. tertiary effects) are well documented in humans[8,9], our understanding of how allostasis and allostatic load are linked and manifests at the cellular level (i.e. primary effects) has remained incomplete. Our *in vitro* findings highlight hypermetabolism as a core manifestation of allostatic load, providing to our knowledge the first quantitative estimate of the energetic cost of allostatic load at the cellular level. Furthermore, our longitudinal data using well-established and validated aging markers in humans such as telomere length and epigenetic clocks, also links hypermetabolism to accelerated aging biology, as conserved features of cellular allostatic overload. Thus, our finding that a stressor (i.e., glucocorticoid signaling) triggers energetically-dependent allostatic recalibrations, which subsequently translate into allostatic overload manifesting as cellular aging aligns well with the original allostatic load model of chronic stress from McEwen and Stellar[78] and with recent evidence of chronic stress pathophysiology in humans[23].

Previous work in cultured rat neurons indicated that GC signaling could influence mitochondrial bioenergetics over hours and days[12], providing a basis for our first hypothesis that chronic GC stress could have long-term bioenergetic consequences. Our cellular lifespan data allowed us to quantify the long-term, persistent cost of the anticipatory allostatic load. With chronic glucocorticoid signaling, it costed fibroblasts more energy to sustain life (+62%), and remarkably more to undergo each cell division (+108%). Plotting total energy consumption together with cell death also revealed a striking shift – potentially reflecting the transition from allostatic load to allostatic overload, where hypermetabolism and cell death were closely associated. Further work will be required to establish whether there is a causal connection between hypermetabolism and fibroblast mortality. We note that relative to Dex, the partial re-routing of metabolic flux to glycolysis with mitoNUITs reduced the slope of the association between hypermetabolism and death by 61.8% ($p<0.001$, **Fig 9K**). This relatively substantial shift may point to adaptive processes whereby cells are able to tolerate higher levels of hypermetabolism when deriving a portion of their energetic needs through both major pathways (OxPhos and glycolysis), rather than through a single pathway. Nevertheless, our findings highlight the primary importance of total energy expenditure rather than of either pathway as a potential driver of allostatic overload.

Because our *in vitro* system consists of isolated cells, the observed effects must be cell autonomous – meaning that they occur independent of inter-organ crosstalk, of the brain, and of other stress mediators encountered *in vivo*. This supports the idea that allostatic load is not a unique phenomenon of complex, multi-organ organisms. Instead, our findings support the notion that allostatic load and allostatic overload are conserved processes able to manifest at the single cell level, whose evolution must therefore have predated the evolution of the brain[79].

These results also open up important questions regarding the mechanisms whereby chronic GC stress cause hypermetabolism. Our data directly rules out two major potential confounders, namely cell volume and division rate. Larger and faster dividing cells would require greater ATP demand. But in fact, chronically stressed cells under allostatic load were significantly smaller and divided significantly more slowly (possibly as an attempt to curtail the rising energetic cost arising from the chronic activation of allostatic responses). Chronic Dex treatment also did not cause uncoupling of mitochondrial OxPhos, which rules out impaired OxPhos coupling efficiency as a cause of hypermetabolism in this model, and instead implicates other active cellular processes as potential contributors for the increased “load” or energetic cost of living.

This state of hypermetabolism is likely driven not by a single process or signaling pathway, but by a multitude of inter-related processes. The major energetic costs within cells arise from gene transcription and translation[80,81], from the maintenance of the plasma membrane potential, and from additional costs arising from the secretion of proteins/cytokines[82]. The biogenesis of organelles is also expected to consume large amounts of ATP. This is particularly true of mitochondria, which are made of large proteomes whose synthesis entail substantial energy expenditure and require genome replication[83]. Mitochondrial OxPhos dysfunction and the heteroplasmic mixture of mutant and normal mtDNA molecules caused by mtDNA instability is predicted to directly increase the energetic cost of organelle maintenance[84]. This cost may be particularly substantial in cells that upregulate mitochondrial biogenesis to build and sustain spare OxPhos capacity in excess of basal needs, as in our chronically stressed fibroblasts. Adding to these maintenance costs, our results revealed elevated extracellular secretion of cytokines and mtDNA during allostatic load. Thus, the increases in mtDNAcn, the modest levels of mtDNA heteroplasmy, and secretion-related costs observed across the lifespan may all contribute to the increased energetic cost of living in Dex-treated fibroblasts. Additional work is required to determine the specific sequence of events leading to hypermetabolism with allostatic load, and the degree to which chronic psychosocial stress trigger hypermetabolism in whole animals, including in humans.

Another open question concerns the link between the allostatic recalibrations underlying hypermetabolism and the reduced lifespan that reflect allostatic overload. Our data cannot definitively establish directionality: does hypermetabolism cause the premature aging phenotype, or do aging biology processes drive increased energy expenditure? Nevertheless, to begin addressing this question we can consider two relevant literatures: allometric scaling of metabolic rates and lifespan, and prospective studies of energy expenditure and mortality in humans. First, among animals there are well-defined relationships among body size, energy expenditure, and aging. These relationships show that animals of smaller sizes (e.g., mice, shrews) have correspondingly higher metabolic rates, age faster, and predictably live shorter lives than larger mammals (e.g., elephants)[85-87]. Body weight and lifespan between animal species also scale linearly with the rate of telomere shortening, meaning that smaller animals with higher metabolic rates exhibit correspondingly faster telomere shortening rates[88]. These inter-species regularities, to which there are notable exceptions, are analogous to our human fibroblast data where Dex-induced allostatic load shifted cells towards a smaller effective size, correspondingly accelerated their metabolic rates, and accelerated the rate of telomere shortening and epigenetic aging), predictably resulting in shortened lifespan.

A second relevant body of literature prospectively links hypermetabolism, measured as elevated basal metabolic rate (BMR), with health outcomes and mortality in humans. Among healthy individuals, independently of well-recognized risk factors such as age, body mass index, smoking, white blood cell count, and diabetes, hypermetabolism is associated with poor health in older individuals[89], and predicts earlier mortality over the subsequent 20-25 years[90,91]. Similarly, in patients with various illnesses (hepatitis B, amyotrophic lateral sclerosis, type 2 diabetes, and cancers), hypermetabolism also predicts worse prognosis and mortality[92-95]. Thus, we propose a model where hypermetabolism reflects the magnitude of allostatic load – i.e., how much energy cells and organisms are expending to maintain stable physiology – which subsequently drives the severity of allostatic load that contribute to accelerated aging and early mortality. Further studies are required to establish the directionality and modifiability of this stress-aging cascade.

In relation to aging biology, our study makes two noteworthy observations. First, it confirms the usefulness of replicative cellular lifespan models[96-98] with high temporal resolution sampling as an experimental approach to quantify the chronic effects of allostasis on a number of cellular, bioenergetic, and molecular outcomes, in a human system. Moreover, deploying aging biomarkers validated in human populations to this *in vitro* system directly contributes to the interpretability of our findings, and to their potential physiological significance. Second, our relative telomere length data revealed that the loss of telomeric repeats is not a fixed quantity per genome duplication event (i.e., cell division), but that these can be decoupled by stress exposure. The accelerated erosion of telomeric repeats per cell division caused by Dex implicate an effect of GC-mediated allostasis on genomic stability, or on other aspects of telomere maintenance. Another study of Dex-treated human fibroblasts reported no effect of cortisol or Dex on the rate of telomere shortening *per day in culture* (one fibroblast line, aged for up to 51 days)[99]. Our study (three donors, aged for up to 250 days) agrees with this observation when telomere shortening is expressed per day in culture. However, taking into account the slowed rate of cell division per day revealed a markedly accelerated rate of shortening per event genome replication, which we regard as the most relevant independent variable to understand telomere maintenance.

Finally, some limitations of this study should be noted. While the epigenetic clocks can act as accurate molecular biomarkers of epigenetic age in several cell types and models, they still face challenges that make them less accurate in some models[62]. Here, we used an approach based on a principal components-adjustment of the epigenetic clocks – PC clocks, which markedly improves the accuracy of the classic DNAm clocks[72]. In relation to our cellular model, compared to convenient immortalized cell lines, or to an experimental design that would include a single arbitrarily chosen donor, we noted substantial inter-individual variation among several measures between our three donors; Donor 1 was least affected whereas Donor 3 was most affected on several variables. This variability likely reflects true inter-individual differences. Thus, although this multi-donor design increases experimental variability, it importantly guards against overfitting results and findings to a single donor/cell line, and therefore provides a more robust test of generalizability for our main findings. We also acknowledge that Dex is a simplistic model of stress, whereas chronic psychosocial stressors in humans involves the action of multiple hormones and metabolic factors. Therefore, although this targeted glucocorticoid stressor provides a strong proof-of-concept of the cell-autonomous energetic and molecular consequences of allostatic load, additional studies with other (combination of) stress mediators are warranted. Finally, our analyses of the RNA sequencing and DNA methylation omics datasets are only partial, and more complete analyses of these data beyond the scope of the present manuscript could yield further insights into the global, longitudinal recalibrations and mechanisms underlying glucocorticoid-driven cellular allostatic load and the resulting allostatic overload. To examine these and related questions, we make available as a community resource the multi-omics dataset of chronic Dex (as well as other treatments, see *Data Availability Statement*)[26].

In summary, we have defined the cell-autonomous features of GC-induced allostatic load, and mapped the long-term consequences associated with cellular allostatic overload in primary human fibroblasts. Our work quantifies the added energetic costs of chronic anticipatory responses at the cellular level, thereby defining hypermetabolism as a feature of allostatic load. We have also documented features of mitochondrial allostatic overload including accelerated telomere shortening and epigenetic aging per cell division. We also describe a robust and specific temporal association between hypermetabolism and premature cell death, aligning with *in vivo* human literature where hypermetabolism increases mortality. Elucidating the mechanisms linking stress exposure, hypermetabolism, and shortened cellular lifespan will require further experimental work, and subsequent extension to well-controlled studies in humans. Resolving the bioenergetic and cellular basis of allostatic load and chronic stress biology should reveal novel bioenergetic principles that can subsequently be leveraged to increase human resilience across the lifespan.

Methods

Human fibroblasts

Primary human fibroblasts of 3 healthy donors were obtained from certified distributors and described in detail in [26]. The characteristics of the three cell lines are summarized in Table 1.

Table 1. Primary human fibroblast information

	Distributor	Catalog #	Genetic	Sex	Ethnicity	Age	Biopsy	Passage	Cell Line ID[1]
Donor 1	Lifeline Cell Technology	FC-0024 Lot # 03099	Normal	Female	Caucasian	18 years	Dermal Breast	1	HC2 (hFB13)
Donor 2	Lifeline Cell Technology	FC-0024 Lot # 00967	Normal	Male	Caucasian	18 years	Dermal Breast	1	HC1 (hFB12)
Donor 3	Coriell Institute	AG01439	Normal	Male	Black	Newborn	Foreskin	4	HC3 (hFB14)

Tissue culture

Cells were cultured under standard conditions of atmospheric O_2, 5% CO_2 and 37°C in DMEM (Thermo Fisher Scientific #10567022) supplemented with 10% Fetal Bovine Serum (FBS, Thermo Fisher Scientific), 50 µg/mL uridine (Sigma-Aldrich), 1% MEM non-essential amino acids (Thermo

---

[1] Refers to the ID given in the Cellular Lifespan Study Shiny Application (See *Data availability statement)*

Fisher Scientific), and 10 μM-1.7 μM palmitate-BSA conjugate (Sigma-Aldrich). Treatment with dexamethasone (Dex, Sigma-Aldrich #D4902, 100 nM) and Dex plus the Mitochondrial Nutrients Uptake InhibiTors cocktail (Dex+mitoNUITs) began after 15-days of culturing post-thaw to allow the cells to adjust to the *in vitro* environment and were dosed every passage. The mitoNUITs cocktail included i) UK5099 (Sigma-Aldrich #PZ0160, 2 μM), an inhibitor of the mitochondrial pyruvate carrier (MPC) that interferes with the pyruvate import into the mitochondrial matrix ii) Etomoxir (Sigma-Aldrich #E1905, 4 μM), an inhibitor of carnitine palmitoyltransferase-1 (CPT-1) that interferes with the fatty-acid-derived Acyl-CoA import into the mitochondrial matrix; and iii) BPTES (Sigma-Aldrich #SML0601, 3 μM), an inhibitor of glutaminase 1 (GLS1) that prevents the conversion of glutamine to glutamate into the mitochondrial matrix. The combined action of these three compounds ultimately abates the availability of the tricarboxylic acid cycle (TCA) substrates Acetyl-CoA and α-ketoglutarate.

Cells were passaged every 5 ± 1 days through standard procedure using Trypsin-EDTA 0.25% (Sigma-Aldrich #T4049). Cell counts and cell volume assessment were performed using 0.4% Trypan Blue Stain and the Countess II Automated Cell Counter (Thermo Fisher Scientific #AMQAF1000). Total cell counts were used to calculate the doubling rate at each passage, and to determine the number cells needed seeded to reach ~90% cell confluency by the time of the following passage. Cells not used for seeding or bioenergetic measurements were stored at -80°C for future analysis. Individual cell lines were terminated after exhibiting less than one population doubling over a 30-day period. The Hayflick limit was calculated as the cumulative number of population doublings of a cell line after termination. Brightfield microscopy images were obtained right before passaging using an inverted phase-contrast microscope (10X and 20X magnification, Thermo Fisher Scientific).

Mycoplasma testing was performed according to the manufacturer's instructions (R&D Systems) on media samples at the end of lifespan for each treatment and cell line used. All tests were negative.

Bioenergetic parameters

The Seahorse XF Cell Mito Stress Test was performed in a XFe96 Seahorse extracellular flux analyzer (Agilent). ATP production rates derived from glycolysis ($J_{\text{ATP-Glyc}}$) and oxidative phosphorylation (OxPhos, $J_{\text{ATP-OxPhos}}$) were calculated from simultaneous measurements of cellular oxygen consumption rate (OCR) and extracellular acidification rate (ECAR) on a monolayer of 20,000 cells, with 10-12 replicates per group. The experimental conditions were, in sequence, as follows: i) 1 μM oligomycin-A, ii) 4 μM FCCP, and iii) 1 μM rotenone and 1 μM antimycin-A (Sigma-Aldrich). Raw OCR and ECAR measurements were normalized by a Hoechst-based cell count for each well (Cytation1 Cell Imager, BioTek), which provided more robust (i.e., less well-to-well variation) and stable results than results normalized to protein content. As illustrated in **Extended Data Figure 1**, Basal OCR, basal ATP-linked

OCR, proton leak OCR, maximal OCR, maximal ATP-linked OCR, compensatory OCR, coupling efficiency, basal ECAR, maximal ECAR, and compensatory ECAR were then utilized to derive ATP production rates from glycolysis and OxPhos as described previously by Mookerjee et al[33]. OCR and ECAR measurements in the absence of glucose (0mM) or with 2-deoxyglucose (2-DG) were performed to confirm the specificity of the ECAR signal in control primary human fibroblasts under these culture conditions[27], indicating that >XX% of the ECAR signal is glucose-dependent.

mtDNA copy number

Cellular DNA was extracted using DNeasy Blood and Tissue Kit (Qiagen #69504). Duplex qPCR reactions with Taqman chemistry were used to quantify mitochondrial (mtDNA, ND1) and nuclear (nDNA, B2M) amplicons, as described previously[100]. Primers and probes utilized were the following: ND1-Fwd: [5'-GAGCGATGGTGAGAGCTAAGGT-3'], ND1-Rev: [5'-CCCTAAAACCCGCCACATCT-3'], ND1-Probe: [5'-/5HEX/CCATCACCC/ZEN/TCTACATCACCGCCC/2IABkGQ/-3']; B2M-Fwd: [5'-TCTCTCTCCATTCTTCAGTAAGTCAACT-3'], B2M-Rev: [5'-CCAGCAGAGAATGGAAAGTCAA-3', B2M-Probe: 5'-/56-FAM/ATGTGTCTG/ZEN/GGTTTCATCCATCCGACCA/3IABkFQ/-3']. Each sample was evaluated in triplicates. Triplicates with average Ct >33 were discarded. Triplicates with C.V. > 10% were also discarded. mtDNA copy number (mtDNAcn) was calculated as $2^{\Delta Ct}$ x 2, where ΔCt = average nDNA Ct - average mtDNA Ct.

mtDNA deletions and point mutations

Long-range PCR (LR-PCR) was performed with mtDNA extracted as described in the mtDNA copy number section. Isolated DNA was amplified by PCR using Hot Start TaKaRa LA Taq kit to yield a 10-Kb product (Takara Biotechnology, #RR042A). Primers utilized were the following: Fwd: [5'-AGATTTACAGTCCAATGCTTC-3'], Rev: [5'-AGATACTGCGACATAGGGTG-3']. PCR products were separated on 1% agarose gel electrophoresis in 1X TBE buffer, stained with GelGreen (Biotium #41005), and imaged using a GelDoc Go Imager (Biorad).

mtDNA next-generation sequencing was used to identify and quantify deletions and point mutations. The entire mtDNA was obtained through the amplification of two overlapping fragments by LR-PCR, using Kapa Long Range DNA polymerase according to the manufacturer's recommendations (Kapa Biosystems). The primer pairs utilized were tested first on Rho zero cells, devoid of mtDNA, to remove nuclear-encoded mitochondrial pseudogene (NUMTS) amplification. Primers utilized were the following: PCR1: Fwd: [5'-AACCAAACCCCAAAGACACC-3'], Rev: [5'-GCCAATAATGACGTGAAGTCC-3']; PCR2: Fwd: [5'-TCCCACTCCTAAACACATCC-3'], Rev: [5'-TTTATGGGGTGATGTGAGCC-3']. PCR products were separated on a 1% agarose gel electrophoresis and NGS Libraries were generated using an enzymatic DNA fragmentation approach with Ion Xpress Plus Fragment Library Kit (Thermo Fisher Scientific). Sequencing was performed using an Ion Torrent S5XL platform with an Ion 540 chip, and signal processing and base calling were performed through the pre-processing embedded pipeline. Demultiplexed reads were mapped according to the mtDNA reference sequence (NC_012920.1), and further analysis was performed through the eKLIPse pipeline[55] (https://github.com/dooguypapua/eKLIPse).

RNA sequencing and transcriptomic analysis

Cells were lysed and stored at -80°C in TRIzol (Thermo Fisher Scientific). RNA isolation of all samples was performed as a single batch using a RNeasy Kit (Qiagen). All samples had an RNA integrity number (RIN) score >8.0, a A260/A280 ratio between 1.8-2.2, and no detectable levels of DNA. cDNA library was prepared from 1,500 ng of RNA using QIAseq FastSelect –rRNA HMR Kit (Qiagen) and NEBNext® Ultra™ II RNA Library Prep Kit for Illumina (New England Biolabs). cDNA was sequenced using paired-end 150 bp chemistry on a HiSeq 4000 System (Illumina) and yielded an average sequencing depth of 40 million reads per sample. Sequenced reads were aligned using the pseudoalignment tool kallisto[101] (v0.44.0) and imported using the 'tximport' package[102] (v1.18.0). Variance stabilizing transformation (VST) was performed using the 'DEseq2' package[103] (v1.30.1). Heatmaps and time courses show transcript levels as the Log_2 of fold change (Log_2FC) of normalized expression relative to the corresponding control time point for each donor. Categorized genes were selected using MitoCarta 3.0[104] and related literature on mitochondrial biogenesis[34-37].

Cell-free DNA

Culture media was collected and stored at -80°C until analyzed as a single batch. Total cell-free DNA (cf-DNA) was isolated from 75 µL f cell culture media using an automated, high throughput methodology previously published[105], using the MagMAX Cell-Free DNA Isolation Kit based on MagMAX™ magnetic-bead technology (Thermo Fisher Scientific). Duplex qPCR reactions with Taqman chemistry were used to simultaneously quantify mitochondrial (cf-mtDNA, ND1) and nuclear (cf-nDNA, B2M) amplicons, using the same primers and probes described in the *mtDNA copy number* section. Serial dilutions of pooled human placenta DNA were used as a standard curve. mtDNA and nDNA copy number (copies/µL) of the standard curve samples were measured using a single-plex Digital PCR (dPCR) for ND1 and B2M genes. The obtained values were then used to calculate the copy number of the experimental samples.

Cytokines

Cytokine levels measurements were performed on the same culture media samples used for cf-DNA measurements. Two multiplex fluorescence-based arrays (R&D) were custom-designed with selected cytokines and chemokines whose levels in human plasma had been reported to be correlated with chronological age[48]. Media samples were run along with negative controls (fresh untreated media), positive controls (healthy fibroblast aged for >200 days), and a standard curve following manufacturer's instructions (Luminex). Positive (>200 days aged healthy fibroblast) and negative controls (fresh untreated media) samples were included along the experimental samples. Cytokine concentrations were then normalized to the number of cells counted at the time of collection to produce estimates of cytokine production on a per-cell basis.

Relative telomere length

Relative telomere length was evaluated on the same genomic material used for other DNA-based measurements. Measurements were performed by single-plex qPCR reactions with SYBR Green chemistry and expressed as the ratio of telomere to single-copy gene abundance (T/S ratio), as previously described[106,107]. Primers utilized for the telomere (T) PCR were: tel1b: [5'-CGGTTT(GTTTGG)$_5$GTT-3'], and tel2b: [5'-GGCTTG(CCTTAC)$_5$CCT-3']. Primers utilized for the single-copy gene (human beta globin) PCR were: Fwd: [5' GCTTCTGACACAACTGTGTTCACTAGC-3'] and Rev: [5'-CACCAACTTCATCCACGTTCACC-3']. Each sample was evaluated in triplicates. Triplicates were subjected to Dixon's Q test for outlier removal, and averaged values of T and S were used to calculate the T/S ratios. T/S ratio for each sample was measured twice. When duplicates showed C.V. > 7%, the sample was run a third time and the two closest values were used.

DNA methylation and DNAmAge

Global DNA methylation was evaluated on the same genomic material used for other DNA-based measurements. DNA samples were submitted to the UCLA Neuroscience Genomic Core (UNGC) for bisulfite conversion and hybridization using the Infinium Methylation EPIC BeadChip kit (Illumina). DNA methylation data was processed in R (v4.0.2), using the 'minfi' package[108] (v1.36.0). Data was normalized using functional normalization (Fun Norm), and RCP and ComBat adjustments were applied using the 'sva' package[109] (v3.12.0) to correct for probe-type and plate bias, respectively.

Original DNAmAge was calculated using the online calculator (https://dnamage.genetics.ucla.edu/new) with normalization, using the age of the donor as the input age. This outputted the Horavth1 (i.e., PanTissue clock), Horvarth2 (i.e., Skin&Blood clock), PhenoAge, Hannum, and GrimAge estimated DNAmAges. More recent versions of the epigenetic clocks based on shared extracted variances among CpGs from principal components were also computed, yielding the

PC-adjusted DNAmAges for each clock[72]. Stable estimates of the rate of epigenetic aging were obtained from the linear regression for each cell line between 27 to 210 days of growth, yielding three values per treatment condition.

Statistical analyses

All statistical analyses were performed using GraphPad Prism (v9.0) and R (v4.0.2) using RStudio (v1.3.1056). All analyses were restricted to matching timepoints between control and the Dex or Dex+mitoNUITs treatments from the CellularLifespan dataset [26]. In graphs of lifespan trajectories, datapoints are connected using the Akima spline curve. Lifespan average graphs show each passage as a single datapoint, and bars represents mean ± standard error of the mean (SEM). The percent differences between groups (i.e., Control vs Dex; or Dex vs mitoNUITs) was computed separately for each cell line (i.e., Donors 1, 2, 3), and groups were compared by two-way ANOVA treating each timepoint as a unique observation. Analyses of gene expression (i.e., HK2, PFK, UQCRC1, COX7A1, POLQ, PPARGC1A, and NRIP1, TPP1, TERC) were similarly performed by two-way ANOVA across all donors, without adjustment for multiple comparisons. To analyze temporal associations between variables, we performed linear regression for each group, and correlation coefficients are Pearson r, squared to obtain proportions of shared variance between variable pairs. To estimate the average expression of transcriptional pathways, the average Log_2 fold change values of each gene were averaged across all timepoints of the lifespan of three donors, and p values obtained using a one-sample t-test against the reference value = 0 (i.e., no change in expression relative to control). For analyses of the Hayflick limit, doubling rate, telomere shortening rate, and epigenetic aging rate, a single value (e.g., slope across the lifespan) was obtained per donor (total n=3), and group averages were compared using ratio paired t-test (two-tailed). Because of the small sample sizes for these outcomes the p values are less reliable than the estimated differences (%) across multiple aging biomarkers. The significance threshold for all analyses was arbitrarily set at 0.05, and effect sizes are provided throughout.

Supplementary Material

Extended Data Figures 1-10 and Supplemental Figures 1-2 are available in the supplemental material.

Author contributions

G.S., and M.P. designed experiments; G.S. performed cellular lifespan studies; A.M. performed quality control experiments; B.S.S. performed alignment and quality control of transcriptomic data; G.S. measured mtDNAcn; S.A.D. and B.K. measured cf-mtDNA; K.R.K. performed cytokine arrays and LR-PCR; C.B., V.P., G.L. performed mtDNA sequencing; J.L. and E.S.E. measured telomere length; S.H., A.H.C., and M.L. contributed the original and PC-DNAm clocks; G.S and N.B.A curated the database; N.B.A. analyzed and interpreted the data with G.S. and M.P; N.B.A. prepared the figures; N.B.A. drafted the manuscript with G.S. and M.P. All authors reviewed the final version of the manuscript.

Funding

This work was supported by the Wharton Fund, NIH grants GM119793 and AG066828 to M.P.

Data availability statement

All data presented in this manuscript are available for download at our Cellular Lifespan Study shiny app: https://columbia-picard.shinyapps.io/shinyapp-Lifespan_Study, with additional data described in [26]. Source data and fibroblast images are available at https://doi.org/10.6084/m9.figshare.18441998.v2 and https://doi.org/10.6084/m9.figshare.18444731.v1, respectively. The raw RNA sequencing and DNA methylation are available at GEO superseries #GSE179849. All code r script for data preprocessing is available at https://github.com/gav-sturm/Cellular_Lifespan_Study. Other information is available upon request from the corresponding author.

References

1 Sterling, P. & Eyer, J. *Allostasis: a new paradigm to explain arousal pathology. In: Fisher S, Reason J, eds. Handbook of Life Stress, Cognition and Health. New York, NY: John Wiley & Sons; 1988:629–649.*, 629–649 (John Wiley & Sons, 1988).

2 Weiner, H. & Mayer, E. [The organism in health and disease. On the path to an integrated biomedical model: sequelae of the theory of psychosomatic medicine]. *Psychother Psychosom Med Psychol* **40**, 81-101 (1990).

3 BS, M. & E, S. Stress and the individual: mechanisms leading to disease. *Arch Intern Med* **153**, 2093-2101 (1993).

4 McEwen, B. S. Protective and damaging effects of stress mediators. *N Engl J Med* **338**, 171-179, doi:10.1056/NEJM199801153380307 (1998).

5 Neufer, P. D. *et al.* Understanding the Cellular and Molecular Mechanisms of Physical Activity-Induced Health Benefits. *Cell Metab* **22**, 4-11, doi:10.1016/j.cmet.2015.05.011 (2015).

6 Flockhart, M. *et al.* Excessive exercise training causes mitochondrial functional impairment and decreases glucose tolerance in healthy volunteers. *Cell Metab* **33**, 957-970 e956, doi:10.1016/j.cmet.2021.02.017 (2021).

7 McEwen, B. S. & Wingfield, J. C. The concept of allostasis in biology and biomedicine. *Horm Behav* **43**, 2-15, doi:10.1016/s0018-506x(02)00024-7 (2003).

8 Gruenewald, T. L., Seeman, T. E., Ryff, C. D., Karlamangla, A. S. & Singer, B. H. Combinations of biomarkers predictive of later life mortality. *Proc Natl Acad Sci U S A* **103**, 14158-14163, doi:10.1073/pnas.0606215103 (2006).

9 Juster, R. P., McEwen, B. S. & Lupien, S. J. Allostatic load biomarkers of chronic stress and impact on health and cognition. *Neurosci Biobehav Rev* **35**, 2-16, doi:10.1016/j.neubiorev.2009.10.002 (2010).

10 Picard, M., McEwen, B. S., Epel, E. S. & Sandi, C. An energetic view of stress: Focus on mitochondria. *Front Neuroendocrinol* **49**, 72-85, doi:10.1016/j.yfrne.2018.01.001 (2018).

11 Basan, M. *et al.* Overflow metabolism in Escherichia coli results from efficient proteome allocation. *Nature* **528**, 99-104, doi:10.1038/nature15765 (2015).

12 Du, J. *et al.* Dynamic regulation of mitochondrial function by glucocorticoids. *Proceedings of the National Academy of Sciences* **106**, 3543-3548, doi:10.1073/pnas.0812671106 (2009).

13 Picard, M. *et al.* Mitochondrial functions modulate neuroendocrine, metabolic, inflammatory, and transcriptional responses to acute psychological stress. *Proceedings of the National Academy of Sciences* **112**, E6614-E6623, doi:10.1073/pnas.1515733112 (2015).

14 Manoli, I. *et al.* Mitochondria as key components of the stress response. *Trends in Endocrinology & Metabolism* **18**, 190-198, doi:10.1016/j.tem.2007.04.004 (2007).

15 Picard, M., Juster, R.-P. & Mcewen, B. S. Mitochondrial allostatic load puts the 'gluc' back in glucocorticoids. *Nature Reviews Endocrinology* **10**, 303-310, doi:10.1038/nrendo.2014.22 (2014).

16 John, S. *et al.* Chromatin accessibility pre-determines glucocorticoid receptor binding patterns. *Nature Genetics* **43**, 264-268, doi:10.1038/ng.759 (2011).

17 Psarra, A.-M. G. & Sekeris, C. E. Glucocorticoids induce mitochondrial gene transcription in HepG2 cells. *Biochimica et Biophysica Acta (BBA) - Molecular Cell Research* **1813**, 1814-1821, doi:10.1016/j.bbamcr.2011.05.014 (2011).

18 Trumpff, C. *et al.* Acute psychological stress increases serum circulating cell-free mitochondrial DNA. *Psychoneuroendocrinology* **106**, 268-276, doi:10.1016/j.psyneuen.2019.03.026 (2019).

19 Lupien, S. J. *et al.* Cortisol levels during human aging predict hippocampal atrophy and memory deficits. *Nature Neuroscience* **1**, 69-73, doi:10.1038/271 (1998).

20 Hackett, R. A. & Steptoe, A. Type 2 diabetes mellitus and psychological stress — a modifiable risk factor. *Nature Reviews Endocrinology* **13**, 547-560, doi:10.1038/nrendo.2017.64 (2017).

21 Ouanes, S. & Popp, J. High Cortisol and the Risk of Dementia and Alzheimer's Disease: A Review of the Literature. *Front Aging Neurosci* **11**, 43, doi:10.3389/fnagi.2019.00043 (2019).

22 Epel, E. S. The geroscience agenda: Toxic stress, hormetic stress, and the rate of aging. *Ageing Research Reviews* **63**, 101167, doi:10.1016/j.arr.2020.101167 (2020).

23 Harvanek, Z. M., Fogelman, N., Xu, K. & Sinha, R. Psychological and biological resilience modulates the effects of stress on epigenetic aging. *Translational Psychiatry* **11**, doi:10.1038/s41398-021-01735-7 (2021).

24 Gold, S. M. *et al.* Comorbid depression in medical diseases. *Nature Reviews Disease Primers* **6**, doi:10.1038/s41572-020-0200-2 (2020).

25 Sturm, G. *et al.* Human aging DNA methylation signatures are conserved but accelerated in cultured fibroblasts. *Epigenetics* **14**, 961-976, doi:10.1080/15592294.2019.1626651 (2019).

26 Sturm, G. *et al. A Multi-Omics and Bioenergetics Longitudinal Aging Dataset in Primary Human Fibroblasts with Mitochondrial Perturbations* (bioRxiv 2021).

27 Sturm, G. *et al. OxPhos Dysfunction Causes Hypermetabolism and Reduces Lifespan in Cells and in Patients with Mitochondrial Diseases* (bioRxiv, 2021).

28 Passow, C. N., Greenway, R., Arias-Rodriguez, L., Jeyasingh, P. D. & Tobler, M. Reduction of Energetic Demands through Modification of Body Size and Routine Metabolic Rates in Extremophile Fish. *Physiological and Biochemical Zoology* **88**, 371-383, doi:10.1086/681053 (2015).

29 Blanckenhorn, W. U. The Evolution of Body Size: What Keeps Organisms Small? *The Quarterly Review of Biology* **75**, 385-407, doi:10.1086/393620 (2000).

30 Dark, J. & Zucker, I. Seasonal Cycles in Energy Balance: Regulation by Lighta. *Annals of the New York Academy of Sciences* **453**, 170-181, doi:10.1111/j.1749-6632.1985.tb11809.x (1985).

31 Vuarin, P., Dammhahn, M. & Henry, P. Y. Individual flexibility in energy saving: body size and condition constrain torpor use. *Functional Ecology* **27**, 793-799, doi:10.1111/1365-2435.12069 (2013).

32 Boal, R. L. *et al.* Height as a Clinical Biomarker of Disease Burden in Adult Mitochondrial Disease. *The Journal of Clinical Endocrinology & Metabolism* **104**, 2057-2066, doi:10.1210/jc.2018-00957 (2019).

33 Mookerjee, S. A., Gerencser, A. A., Nicholls, D. G. & Brand, M. D. Quantifying intracellular rates of glycolytic and oxidative ATP production and consumption using extracellular flux measurements. *Journal of Biological Chemistry* **292**, 7189-7207, doi:10.1074/jbc.m116.774471 (2017).

34 Schimmel, J., Van Schendel, R., Den Dunnen, J. T. & Tijsterman, M. Templated Insertions: A Smoking Gun for Polymerase Theta-Mediated End Joining. *Trends in Genetics* **35**, 632-644, doi:10.1016/j.tig.2019.06.001 (2019).

35 Wu, Z. *et al.* Mechanisms Controlling Mitochondrial Biogenesis and Respiration through the Thermogenic Coactivator PGC-1. *Cell* **98**, 115-124, doi:10.1016/s0092-8674(00)80611-x (1999).

36 Seth, A. *et al.* The Transcriptional Corepressor RIP140 Regulates Oxidative Metabolism in Skeletal Muscle. *Cell Metabolism* **6**, 236-245, doi:10.1016/j.cmet.2007.08.004 (2007).

37 Powelka, A. M. Suppression of oxidative metabolism and mitochondrial biogenesis by the transcriptional corepressor RIP140 in mouse adipocytes. *Journal of Clinical Investigation* **116**, 125-136, doi:10.1172/jci26040 (2005).

38 Collins, L. V., Hajizadeh, S., Holme, E., Jonsson, I. M. & Tarkowski, A. Endogenously oxidized mitochondrial DNA induces in vivo and in vitro inflammatory responses. *J Leukoc Biol* **75**, 995-1000, doi:10.1189/jlb.0703328 (2004).

39 Stephens, O. R. *et al.* Characterization and origins of cell-free mitochondria in healthy murine and human blood. *Mitochondrion* **54**, 102-112, doi:10.1016/j.mito.2020.08.002 (2020).

40 Sansone, P. *et al.* Packaging and transfer of mitochondrial DNA via exosomes regulate escape from dormancy in hormonal therapy-resistant breast cancer. *Proc Natl Acad Sci U S A* **114**, E9066-E9075, doi:10.1073/pnas.1704862114 (2017).

41 Hummel, E. M. *et al.* Cell-free DNA release under psychosocial and physical stress conditions. *Transl Psychiatry* **8**, 236, doi:10.1038/s41398-018-0264-x (2018).

42 Pinti, M. *et al.* Circulating mitochondrial DNA increases with age and is a familiar trait: Implications for “inflamm-aging”. *European Journal of Immunology* **44**, 1552-1562, doi:10.1002/eji.201343921 (2014).

43 Miliotis, S., Nicolalde, B., Ortega, M., Yepez, J. & Caicedo, A. Forms of extracellular mitochondria and their impact in health. *Mitochondrion* **48**, 16-30, doi:10.1016/j.mito.2019.02.002 (2019).

44 Trumpff, C. *et al.* Stress and circulating cell-free mitochondrial DNA: A systematic review of human studies, physiological considerations, and technical recommendations. *Mitochondrion* **59**, 225-245, doi:10.1016/j.mito.2021.04.002 (2021).

45 Mcewen, B. S. Interacting mediators of allostasis and allostatic load: towards an understanding of resilience in aging. *Metabolism* **52**, 10-16, doi:10.1016/s0026-0495(03)00295-6 (2003).

46 Mccaffery, J. M., Marsland, A. L., Strohacker, K., Muldoon, M. F. & Manuck, S. B. Factor Structure Underlying Components of Allostatic Load. *PLoS ONE* **7**, e47246, doi:10.1371/journal.pone.0047246 (2012).

47 Furman, D. *et al.* Chronic inflammation in the etiology of disease across the life span. *Nature Medicine* **25**, 1822-1832, doi:10.1038/s41591-019-0675-0 (2019).

48 Tanaka, T. *et al.* Plasma proteomic signature of age in healthy humans. *Aging Cell* **17**, e12799, doi:10.1111/acel.12799 (2018).

49 Waage, A., Slupphaug, G. & Shalaby, R. Glucocorticoids inhibit the production of IL 6 from monocytes, endothelial cells and fibroblasts. *European Journal of Immunology* **20**, 2439-2443, doi:10.1002/eji.1830201112 (1990).

50 Picard, M. & Turnbull, D. M. Linking the metabolic state and mitochondrial DNA in chronic disease, health, and aging. *Diabetes* **62**, 672-678, doi:10.2337/db12-1203 (2013).

51 Wang, Y., Guo, X., Ye, K., Orth, M. & Gu, Z. Accelerated expansion of pathogenic mitochondrial DNA heteroplasmies in Huntington's disease. *Proc Natl Acad Sci U S A* **118**, doi:10.1073/pnas.2014610118 (2021).

52 Klein, H. U. *et al.* Characterization of mitochondrial DNA quantity and quality in the human aged and Alzheimer's disease brain. *Mol Neurodegener* **16**, 75, doi:10.1186/s13024-021-00495-8 (2021).

53 Picard, M. *et al.* Mitochondrial dysfunction and lipid accumulation in the human diaphragm during mechanical ventilation. *Am J Respir Crit Care Med* **186**, 1140-1149, doi:10.1164/rccm.201206-0982OC (2012).

54 Meissner, C., Bruse, P. & Oehmichen, M. Tissue-specific deletion patterns of the mitochondrial genome with advancing age. *Exp Gerontol* **41**, 518-524, doi:10.1016/j.exger.2006.03.010 (2006).

55 Goudenege, D. *et al.* eKLIPse: a sensitive tool for the detection and quantification of mitochondrial DNA deletions from next-generation sequencing data. *Genet Med* **21**, 1407-1416, doi:10.1038/s41436-018-0350-8 (2019).

56 Spendiff, S. *et al.* Mitochondrial DNA deletions in muscle satellite cells: implications for therapies. *Hum Mol Genet* **22**, 4739-4747, doi:10.1093/hmg/ddt327 (2013).

57 Hayflick, L. The Limited in Vitro Lifetime of Human Diploid Cell Strains. *Exp Cell Res* **37**, 614-636, doi:10.1016/0014-4827(65)90211-9 (1965).

58 Hayflick, L. & Moorhead, P. S. The serial cultivation of human diploid cell strains. *Exp Cell Res* **25**, 585-621, doi:10.1016/0014-4827(61)90192-6 (1961).

59 Yegorov, Y. E., Poznyak, A. V., Nikiforov, N. G., Sobenin, I. A. & Orekhov, A. N. The Link between Chronic Stress and Accelerated Aging. *Biomedicines* **8**, 198, doi:10.3390/biomedicines8070198 (2020).

60 Lin, J. & Epel, E. Stress and telomere shortening: Insights from cellular mechanisms. *Ageing Res Rev* **73**, 101507, doi:10.1016/j.arr.2021.101507 (2021).

61 Horvath, S. & Raj, K. DNA methylation-based biomarkers and the epigenetic clock theory of ageing. *Nature Reviews Genetics* **19**, 371-384, doi:10.1038/s41576-018-0004-3 (2018).

62 Bell, C. G. *et al.* DNA methylation aging clocks: challenges and recommendations. *Genome Biology* **20**, doi:10.1186/s13059-019-1824-y (2019).

63 Lu, A. T. *et al.* DNA methylation-based estimator of telomere length. *Aging* **11**, 5895-5923, doi:10.18632/aging.102173 (2019).

64 Diotti, R. & Loayza, D. Shelterin complex and associated factors at human telomeres. *Nucleus* **2**, 119-135, doi:10.4161/nucl.2.2.15135 (2011).

65 Jacobs, E. G., Epel, E. S., Lin, J., Blackburn, E. H. & Rasgon, N. L. Relationship between leukocyte telomere length, telomerase activity, and hippocampal volume in early aging. *JAMA Neurol* **71**, 921-923, doi:10.1001/jamaneurol.2014.870 (2014).

66 Zalli, A. *et al.* Shorter telomeres with high telomerase activity are associated with raised allostatic load and impoverished psychosocial resources. *Proc Natl Acad Sci U S A* **111**, 4519-4524, doi:10.1073/pnas.1322145111 (2014).

67 Lu, A. T. *et al.* DNA methylation GrimAge strongly predicts lifespan and healthspan. *Aging* **11**, 303-327, doi:10.18632/aging.101684 (2019).

68 Horvath, S. DNA methylation age of human tissues and cell types. *Genome Biology* **14**, R115, doi:10.1186/gb-2013-14-10-r115 (2013).

69 Horvath, S. *et al.* Epigenetic clock for skin and blood cells applied to Hutchinson Gilford Progeria Syndrome and ex vivo studies. *Aging* **10**, 1758-1775, doi:10.18632/aging.101508 (2018).

70 Hannum, G. *et al.* Genome-wide Methylation Profiles Reveal Quantitative Views of Human Aging Rates. *Molecular Cell* **49**, 359-367, doi:10.1016/j.molcel.2012.10.016 (2013).

71 Levine, M. E. *et al.* An epigenetic biomarker of aging for lifespan and healthspan. *Aging* **10**, 573-591, doi:10.18632/aging.101414 (2018).

72 Higgins-Chen, A. T. *et al. A computational solution for bolstering reliability of epigenetic clocks: Implications for clinical trials and longitudinal tracking* (bioRxiv 2021).

73 Kim, Y. *et al.* Mitochondrial Aging Defects Emerge in Directly Reprogrammed Human Neurons due to Their Metabolic Profile. *Cell Reports* **23**, 2550-2558, doi:10.1016/j.celrep.2018.04.105 (2018).

74 Correia-Melo, C. *et al.* Mitochondria are required for pro-ageing features of the senescent phenotype. *EMBO J* **35**, 724-742, doi:10.15252/embj.201592862 (2016).

75 Hildyard, J. C., Ammala, C., Dukes, I. D., Thomson, S. A. & Halestrap, A. P. Identification and characterisation of a new class of highly specific and potent inhibitors of the mitochondrial pyruvate carrier. *Biochim Biophys Acta* **1707**, 221-230, doi:10.1016/j.bbabio.2004.12.005 (2005).

76 Kruszynska, Y. T. & Sherratt, H. S. Glucose kinetics during acute and chronic treatment of rats with 2[6(4-chloro-phenoxy)hexyl]oxirane-2-carboxylate, etomoxir. *Biochem Pharmacol* **36**, 3917-3921, doi:10.1016/0006-2952(87)90458-8 (1987).

77 Robinson, M. M. *et al.* Novel mechanism of inhibition of rat kidney-type glutaminase by bis-2-(5-phenylacetamido-1,2,4-thiadiazol-2-yl)ethyl sulfide (BPTES). *Biochem J* **406**, 407-414, doi:10.1042/BJ20070039 (2007).

78 Mcewen, B. S. Stress and the Individual. *Archives of Internal Medicine* **153**, 2093, doi:10.1001/archinte.1993.00410180039004 (1993).

79 Sterling, P. *What is health? Allostasis and the evolution of human design.* . (The MIT Press, 2020).

80 Kafri, M., Metzl-Raz, E., Jona, G. & Barkai, N. The Cost of Protein Production. *Cell Reports* **14**, 22-31, doi:10.1016/j.celrep.2015.12.015 (2016).

81 Buttgereit, F. & Brand, M. D. A hierarchy of ATP-consuming processes in mammalian cells. *Biochemical Journal* **312**, 163-167, doi:10.1042/bj3120163 (1995).

82 Gutierrez, J. M. *et al.* Genome-scale reconstructions of the mammalian secretory pathway predict metabolic costs and limitations of protein secretion. *Nature Communications* **11**, doi:10.1038/s41467-019-13867-y (2020).

83 Molenaar, D., Van Berlo, R., De Ridder, D. & Teusink, B. Shifts in growth strategies reflect tradeoffs in cellular economics. *Molecular Systems Biology* **5**, 323, doi:10.1038/msb.2009.82 (2009).

84 Hoitzing, H. *et al.* Energetic costs of cellular and therapeutic control of stochastic mitochondrial DNA populations. *PLoS Comput Biol* **15**, e1007023, doi:10.1371/journal.pcbi.1007023 (2019).

85 Rolfe, D. F. & Brown, G. C. Cellular energy utilization and molecular origin of standard metabolic rate in mammals. *Physiol Rev* **77**, 731-758, doi:10.1152/physrev.1997.77.3.731 (1997).

86 West, G. B., Woodruff, W. H. & Brown, J. H. Allometric scaling of metabolic rate from molecules and mitochondria to cells and mammals. *Proc Natl Acad Sci U S A* **99 Suppl 1**, 2473-2478, doi:10.1073/pnas.012579799 (2002).

87 Healy, K. *et al.* Ecology and mode-of-life explain lifespan variation in birds and mammals. *Proceedings of the Royal Society B: Biological Sciences* **281**, 20140298, doi:10.1098/rspb.2014.0298 (2014).

88 Whittemore, K., Vera, E., Martinez-Nevado, E., Sanpera, C. & Blasco, M. A. Telomere shortening rate predicts species life span. *Proc Natl Acad Sci U S A* **116**, 15122-15127, doi:10.1073/pnas.1902452116 (2019).

89 Schrack, J. A., Knuth, N. D., Simonsick, E. M. & Ferrucci, L. "IDEAL" aging is associated with lower resting metabolic rate: the Baltimore Longitudinal Study of Aging. *J Am Geriatr Soc* **62**, 667-672, doi:10.1111/jgs.12740 (2014).

90 Jumpertz, R. *et al.* Higher energy expenditure in humans predicts natural mortality. *J Clin Endocrinol Metab* **96**, E972-976, doi:10.1210/jc.2010-2944 (2011).

91 Ruggiero, C. *et al.* High basal metabolic rate is a risk factor for mortality: the Baltimore Longitudinal Study of Aging. *J Gerontol A Biol Sci Med Sci* **63**, 698-706, doi:10.1093/gerona/63.7.698 (2008).

92 Sampath Kumar, A. *et al.* Correlation between basal metabolic rate, visceral fat and insulin resistance among type 2 diabetes mellitus with peripheral neuropathy. *Diabetes Metab Syndr* **13**, 344-348, doi:10.1016/j.dsx.2018.10.005 (2019).

93 Vazeille, C. *et al.* Relation between hypermetabolism, cachexia, and survival in cancer patients: a prospective study in 390 cancer patients before initiation of anticancer therapy. *Am J Clin Nutr* **105**, 1139-1147, doi:10.3945/ajcn.116.140434 (2017).

94 Steyn, F. J. *et al.* Hypermetabolism in ALS is associated with greater functional decline and shorter survival. *J Neurol Neurosurg Psychiatry* **89**, 1016-1023, doi:10.1136/jnnp-2017-317887 (2018).

95 Yao, J. *et al.* Persistently Increased Resting Energy Expenditure Predicts Short-Term Mortality in Patients with Acute-on-Chronic Liver Failure. *Ann Nutr Metab* **73**, 2-9, doi:10.1159/000487604 (2018).

96 Lowe, D., Horvath, S. & Raj, K. Epigenetic clock analyses of cellular senescence and ageing. *Oncotarget* **7**, 8524-8531, doi:10.18632/oncotarget.7383 (2016).

97 Minteer, C. *et al.* Tick tock, tick tock: Mouse culture and tissue aging captured by an epigenetic clock. *Aging Cell*, doi:10.1111/acel.13553 (2022).

98 Bork, S. *et al.* DNA methylation pattern changes upon long-term culture and aging of human mesenchymal stromal cells. *Aging Cell* **9**, 54-63, doi:10.1111/j.1474-9726.2009.00535.x (2010).

99 Zannas, A. S., Kosyk, O. & Leung, C. S. Prolonged Glucocorticoid Exposure Does Not Accelerate Telomere Shortening in Cultured Human Fibroblasts. *Genes* **11**, 1425, doi:10.3390/genes11121425 (2020).

100 Picard, M. *et al.* Progressive increase in mtDNA 3243A>G heteroplasmy causes abrupt transcriptional reprogramming. *Proceedings of the National Academy of Sciences* **111**, E4033-E4042, doi:10.1073/pnas.1414028111 (2014).

101 Bray, N. L., Pimentel, H., Melsted, P. & Pachter, L. Near-optimal probabilistic RNA-seq quantification. *Nature Biotechnology* **34**, 525-527, doi:10.1038/nbt.3519 (2016).

102 Soneson, C., Love, M. I. & Robinson, M. D. Differential analyses for RNA-seq: transcript-level estimates improve gene-level inferences. *F1000Research* **4**, 1521, doi:10.12688/f1000research.7563.2 (2016).

103 Love, M. I., Huber, W. & Anders, S. Moderated estimation of fold change and dispersion for RNA-seq data with DESeq2. *Genome Biology* **15**, doi:10.1186/s13059-014-0550-8 (2014).

104 Rath, S. *et al.* MitoCarta3.0: an updated mitochondrial proteome now with sub-organelle localization and pathway annotations. *Nucleic Acids Research* **49**, D1541-D1547, doi:10.1093/nar/gkaa1011 (2021).

105 Ware, S. A. *et al.* An automated, high-throughput methodology optimized for quantitative cell-free mitochondrial and nuclear DNA isolation from plasma. *Journal of Biological Chemistry* **295**, 15677-15691, doi:10.1074/jbc.ra120.015237 (2020).

106 Lin, J. *et al.* Analyses and comparisons of telomerase activity and telomere length in human T and B cells: Insights for epidemiology of telomere maintenance. *Journal of Immunological Methods* **352**, 71-80, doi:10.1016/j.jim.2009.09.012 (2010).

107 Cawthon, R. M. Telomere measurement by quantitative PCR. *Nucleic Acids Research* **30**, 47e-47, doi:10.1093/nar/30.10.e47 (2002).

108 Aryee, M. J. *et al.* Minfi: a flexible and comprehensive Bioconductor package for the analysis of Infinium DNA methylation microarrays. *Bioinformatics* **30**, 1363-1369, doi:10.1093/bioinformatics/btu049 (2014).

109 Leek, J. T., Johnson, W. E., Parker, H. S., Jaffe, A. E. & Storey, J. D. The sva package for removing batch effects and other unwanted variation in high-throughput experiments. *Bioinformatics* **28**, 882-883, doi:10.1093/bioinformatics/bts034 (2012).

Figure legends

Figure 1. Longitudinal cytologic effects of chronic glucocorticoid signaling in primary human fibroblasts. (**A**) Study design: primary human fibroblasts derived from three healthy donors (Donors 1, 2, and 3) were cultured under standard conditions (control) or chronically treated with Dexamethasone (Dex, 100 nM) across their lifespan for up to 150-250 days, until replicative senescence. Cytologic parameters were evaluated every 5-7 days, while bioenergetics, DNA, RNA, and secreted factors parameters were evaluated every 10-20 days. (**B**) Representative images of untreated replicating control and Dex-treated cells from Donor 1 at 25 days of treatment. (**C**) Raw lifespan trajectories of cell volume. (**D**) To examine the effects of the chronic glucocorticoid signaling from the effects of aging, lifespan trajectories (left panel) and lifespan average effects (right panel) of Dex treatment on cell volume are expressed relative to the corresponding control time points for each donor. (**E-F**) Same as C-D but for the proportion of dead cells at each passage. n = 3 donors per group, n = 26-36 timepoints per donor. Lifespan average graphs are mean ± SEM, two-way ANOVA. * $p < 0.05$, **** $p < 0.0001$, ns: not significant.

Figure 2. Cellular allostatic load is associated with hypermetabolism. (A-C) Energy expenditure trajectories across the cellular lifespan derived from Seahorse extracellular flux analyzer described in detail in **Extended Data Fig. 1**. (**A**) Lifespan trajectories (left panel) and lifespan average effects (right panel) of Dex treatment expressed relative to the corresponding control time points for each donor on basal glycolysis-derived ATP ($J_{\text{ATP-Glyc}}$), (**B**) OxPhos-derived ATP ($J_{\text{ATP-OxPhos}}$), and (**C**) total ATP production ($J_{\text{ATP-Total}}$) corrected for cell volume. n = 3 donors per group, 8-13 timepoints per donor. Lifespan average graphs are mean ± SEM, two-way ANOVA * $p < 0.05$, ** $p < 0.01$, *** $p < 0.001$, **** $p < 0.0001$, ns: not significant. $J_{\text{ATP-Total}}$ is the algebraic sum of $J_{\text{ATP-Glyc}}$ and $J_{\text{ATP-OxPhos}}$.

Figure 3. Cellular allostatic load involves a metabolic shift towards OxPhos. (**A**) Fraction of basal energy production from $J_{\text{ATP-Glyc}}$ (yellow) and basal $J_{\text{ATP-OxPhos}}$ (green) across the lifespan. (**B**) Compensatory glycolytic capacity, expressed as the percentage of basal $J_{\text{ATP-Total}}$, achieved when OxPhos ATP production is inhibited with oligomycin. Basal $J_{\text{ATP-Glyc}}$ levels are shown in dark yellow, and compensatory $J_{\text{ATP-Glyc}}$ are shown in bright yellow. (**C**) Same as B but for spare OxPhos capacity, expressed as the percentage of basal $J_{\text{ATP-OxPhos}}$ that can be achieved under uncoupled condition with FCCP. Basal $J_{\text{ATP-OxPhos}}$ levels are shown in dark green, and spare $J_{\text{ATP-OxPhos}}$ are shown in bright green. (**D**) Correlation between spare $J_{\text{ATP-OxPhos}}$/cell volume and basal $J_{\text{ATP-OxPhos}}$/cell volume (left panel) and between spare $J_{\text{ATP-OxPhos}}$/cell volume and basal $J_{\text{ATP-Total}}$/cell volume (right panel). (**E**) Lifespan trajectories (left panel) and lifespan average effects (right panel) of Dex treatment on coupling efficiency expressed relative to the corresponding control time points for each donor. (**F**) Same as C but for mtDNA

copy number/cell volume. n = 3 donors per group, 8-13 timepoints per donor. Lifespan average graphs are mean ± SEM, two-way ANOVA. Thick lines in correlation graphs show linear regression for each group, Pearson r correlation. ** $p < 0.01$, *** $p < 0.001$, **** $p < 0.0001$, ns: not significant. $J_{\text{ATP-Glyc}}$: ATP production rate derived from glycolysis. $J_{\text{ATP-OxPhos}}$: ATP production rate derived from OxPhos. $J_{\text{ATP-Total}}$: algebraic sum of $J_{\text{ATP-Glyc}}$ and $J_{\text{ATP-OxPhos}}$.

Figure 4. Cellular allostatic load involves transcriptional upregulation of OxPhos and mitochondrial biogenesis. (**A**) Heatmaps showing the effect of Dex treatment on the expression of glycolytic genes, expressed as the Log_2 of fold change (Log_2FC) of normalized gene expression relative to the corresponding control time points for each donor. (**B**) Same as A but for genes encoding the subunits of complexes I, II, III, IV and V of the OxPhos system, (**C**) mtDNA maintenance, (**D**) mtDNA replication, and (**E**) mitochondrial biogenesis. Two key regulators of mitochondrial biogenesis, one positive (PGC-1a) and one negative (NRIP1) are highlighted, showing expression signatures consistent with both activated and un-repressed mitochondrial biogenesis. (**F**) Average effect of Dex treatment shown in A-E. Each datapoint represents the gene average of the Log_2FC values throughout the entire lifespan of the three donors (n=28 timepoints). Average graphs are mean ± SEM, with each gene shown as a single datapoint. One-sample t-test different than 0, * $p < 0.05$, ** $p < 0.01$, *** $p < 0.001$, **** $p < 0.0001$, ns: not significant. n = 3 donors per group, 9-10 timepoints per donor. Heatmap row annotation with individual gene names is provided in *Supplemental Data Figure 1*.

Figure 5. Cellular allostatic load increases cell-free DNA levels. (**A**) Lifespan trajectories (left panel) and lifespan average effects (right panel) of Dex treatment on cell-free mitochondrial DNA (cf-mtDNA) expressed relative to the corresponding control time points for each donor. (**B**) Pearson correlation between cf-mtDNA and the proportion of dead cells at each passage. (**C**) Same as A but for cell-free nuclear DNA (cf-nDNA). (**D**) Same as B but for cf-nDNA. n = 3 donors per group, 6-10 timepoints per donor. Lifespan average graphs are mean ± SEM, two-way ANOVA. Thick lines in correlation graphs show linear regression for each group, Pearson r correlation. * $p < 0.05$, ** $p < 0.01$, *** $p < 0.001$, **** $p < 0.0001$, ns: not significant.

Figure 6. Cellular allostatic load alters cytokine release. (**A**) Heatmaps showing the effect of Dex treatment on the secretion of age-related cytokines, expressed as the Log_2 fold change (Log_2FC) of cytokine concentration (pg/mL of medium), relative to the corresponding control time points for each donor. (**B**) Lifespan trajectories of cytokine concentration in cells treated with Dex relative to the corresponding control time point for each donor. Thin curves in soft red represents individual cytokines; thick curves in red represent the average of all cytokines evaluated; thick lines in gray represent the control level. (**C**) Lifespan trajectories (left panel) and average effects (right panel) of Dex treatment on

TFPII (most upregulated cytokine) levels per mL of culture media expressed relative to the corresponding control time point for each donor. (**D**) Same as C but for IL6 (most downregulated cytokine). n = 3 donors per group, 6-10 timepoints per donor. Lifespan average graphs are mean ± SEM, two-way ANOVA. *** p < 0.001, **** p < 0.0001, ns: not significant. Lifespan trajectories and average effects of Dex treatment on levels of every cytokine detected are shown in **Supplemental Figure 2**.

Figure 7. Cellular allostatic load causes mtDNA instability. (**A**) Long-range PCR (10 kb product) of mtDNA extracted from Donor 2 control and Dex-treated cells across lifespan, resolved by agarose gel electrophoresis. The presence of amplicons of sizes smaller than 10 kb reveal the presence of mtDNA molecules containing deletions. (**B**) Circos plots from mtDNA sequencing and Eclipse analysis for mtDNA extracted from Donor 2 control and Dex-treated cells at days 26, 56 and 126. Each red line represents an individual deletion that spans the sequence contained between its two ends. The line thickness reflects the level of relative abundance or heteroplasmy for each deletion (see **Extended Data Fig. 6** for all donors). (**C**) Lifespan trajectories (*left* panel) and average effects (*right* panel) of Dex treatment on the cumulative heteroplasmy of all deletions present at a particular time point, expressed relative to the corresponding control time point for each donor. (**D**) Lifespan trajectories of individual point mutations heteroplasmy found in control (left panels) and Dex-treated cells (right panels) of the three donors. n = 3 donors per group, 2-8 timepoints per donor. Datapoints in lifespan trajectories are connected using the Akima spline curve, but the datapoints for Donor 3 in (C), for which due to insufficient time points the spline fit was not feasible and therefore datapoints were connected through a straight line. Lifespan average graphs are mean ± SEM, two-way ANOVA. ns: not significant, N/A: not applicable.

Figure 8. Cells under chronic allostatic load display accelerated cellular aging. (**A**) Lifespan trajectories of cumulative population doublings. (**B**) Hayflick limit for each donor of each group. (**C**) Early life doubling rate, calculated as the slope of the linear regression of the population doubling trajectories within the first 50 days of treatment. (**D**) Telomere length across population doublings, with linear regressions for each donor of each group (left panel), and telomere shortening rate calculated as the slope of the correspondent linear regressions (right panel). (**E**) Epigenetic age calculated by the principal components (PC)-adjusted PhenoAge epigenetic clock, with linear regressions for each donor of each group (left panel), and epigenetic aging rate calculated as the slope of the corresponding linear equation (right panel). (**F**) Epigenetic aging rate for the Dex group relative to the control as calculated by all the PC-adjusted epigenetic clocks evaluated: PA: PhenoAge, H: Hannum, S&B: Skin and Blood, PT: PanTissue, GA: GrimAge. Detailed analysis of these epigenetic clocks is in **Extended Data Fig. 9** (**G**) Percentage of dead cells (upper panels) and basal $J_{\text{ATP-Total}}$/cell volume (lower panels) across

population doublings for Donor 1 (left panels), Donor 2 (middle panels) and Donor 3 (right panels). (**H**) Correlation between proportion of dead cells in every passage and Basal $J_{\text{ATP-Total}}$/cell volume. n = 3 donors per group; timepoints per donor: n = 26-36 in A, n = 4-14 in D-E, n = 8-13 in G-H. Bar graphs are mean ± SEM, ratio paired t-test (two-tailed). Thick lines in correlation graphs show linear regression for each group, Pearson r correlation. * $p < 0.05$, ** $p < 0.01$, **** $p < 0.0001$, ns: not significant.

Figure 9. Hypermetabolism, not the metabolic shift towards OxPhos, predicts cell death. (**A**) Energetic phenotype of cells treated with Dex and Dex+mitoNUITs defined by Basal $J_{\text{ATP-OxPhos}}$/cell volume and Basal $J_{\text{ATP-Glyc}}$/cell volume across lifespan. (**B**) Lifespan average effects of Dex+mitoNUIT treatment on $J_{\text{ATP-Total}}$/cell volume. (**C**) Values across lifespan (left panel) and average effects (right panel) of basal $J_{\text{ATP-Glyc}}$ (yellow) and basal $J_{\text{ATP-OxPhos}}$ (green) expressed as percentage of basal $J_{\text{ATP-Total}}$. (**D**) Lifespan trajectories of cumulative population doublings. (**E**) Hayflick limit for each donor of each group. (**F**) Early life doubling rate, calculated as the slope of the linear regression of the population doubling trajectories within the first 50 days of treatment. (**G**) Telomere length across population doublings, with linear regressions for each donor of each group (left panel), and telomere shortening rate calculated as the slope of the correspondent linear regressions (right panel). (**H**) Epigenetic age calculated by the principal components (PC)-adjusted PhenoAge epigenetic clock, with linear regressions for each donor of each group (left panel), and epigenetic aging rate calculated as the slope of the correspondent linear regressions (right panel). (**J**) Epigenetic aging rate for the Dex+mitoNUITs group relative to the Dex group as calculated by all the PC-adjusted epigenetic clocks evaluated: PA: Phone Age, H: Hannum, S&B: Skin and Blood, PT: Pan Tissue, GA: Grimm Age. (**K**) Percentage of dead cells (upper panels) and basal $J_{\text{ATP-Total}}$/cell volume (lower panels) across population doublings for Donor 1 (left panels), Donor 2 (middle panels) and Donor 3 (right panels). (**H**) Correlation between proportion of dead cells in every passage and Basal $J_{\text{ATP-Total}}$/cell volume. n = 3 donors per group; timepoints per donor: n=7-11 in B-C, n = 26-36 in D, n = 4-14 in G-H, n = 8-13 in J-K. Lifespan average graphs are mean ± SEM, two-way ANOVA in B, ratio paired t-test (two-tailed) in E, F, H and I. Thick lines in correlation graphs show linear regression for each group, Pearson r correlation. * $p < 0.05$, ** $p < 0.01$, *** $p < 0.001$, **** $p < 0.0001$, ns: not significant. mitoNUITs: Mitochondrial uptake inhibitors. $J_{\text{ATP-Glyc:}}$ ATP production rate derived from glycolysis. $J_{\text{ATP-OxPhos}}$: ATP production rate derived from OxPhos. $J_{\text{ATP-Total}}$: algebraic sum of $J_{\text{ATP-Glyc}}$ and $J_{\text{ATP-OxPhos}}$.

Figure 10. Summary diagram. Proposed model for the transduction of glucocorticoid signaling into cellular allostatic load and its interrelated cellular features, and the chronic downstream consequences of allostatic overload on cellular aging.

Extended Data Figure 1. Evaluation of bioenergetic parameters. (**A**) Study design: primary human fibroblasts derived from three healthy donors (Donors 1, 2, 3) were cultured under standard conditions or chronically treated with Dexamethasone (Dex, 100 nM) across its lifespan for up to 150-250 days. Bioenergetics parameters were evaluated every 15-10 days performing the Seahorse Mito Stress Test (Agilent). Green bars highlight the cell volume values the day prior to the test, which were then utilized to normalize the bioenergetic parameters. (**B**) Representative curves of cellular oxygen consumption rate (OCR) and extracellular acidification rate (ECAR) obtained throughout the Seahorse Mito Stress Test (**C**)**.** Bioenergetic parameters that can be derived from ECAR and OCR curves in B. $J_{\text{ATP-Glyc}}$: ATP production rate derived from glycolysis. $J_{\text{ATP-OxPhos}}$: ATP production rate derived from OxPhos. O: Oligomycin. FCCP: Carbonyl cyanide-p-trifluoromethoxyphenyl-hydrazon. R/A: Rotenone/Antimycin A.

Extended Data Figure 2. Effects of chronic glucocorticoid signaling on basal bioenergetic parameters on a per cell basis. (A) Lifespan trajectories (*left* panel) and lifespan average effects (*right* panel) of Dex treatment on basal $J_{\text{ATP-Glyc}}$ /20k cells expressed relative to the corresponding control time points for each donor. (**B**) Same as A but for $J_{\text{ATP-OxPhos}}$/20k cells. (**C**) Same as A but for $J_{\text{ATP-Total}}$/20k cells. (**D**) Correlation between basal $J_{\text{ATP-Total}}$ and basal $J_{\text{ATP-Glyc}}$ (*left* panel) and between basal $J_{\text{ATP-Total}}$ and basal $J_{\text{ATP-OxPhos}}$ (*right* panel). n = 3 donors per group, 8-13 timepoints per donor. Lifespan average graphs are mean ± SEM, two-way ANOVA. Thick lines in correlation graphs show linear regression for each group, Pearson r correlation. ** $p < 0.01$, *** $p < 0.001$, **** $p < 0.0001$, ns: not significant. $J_{\text{ATP-Glyc}}$: ATP production rate derived from glycolysis. $J_{\text{ATP-OxPhos}}$: ATP production rate derived from OxPhos. $J_{\text{ATP-Total}}$: algebraic sum of $J_{\text{ATP-Glyc}}$ and $J_{\text{ATP-OxPhos}}$.

Extended Data Figure 3. Effects of chronic glucocorticoid signaling on mtDNAcn. (**A**) Lifespan trajectories of Dex treatment on mtDNA copy number (mtDNAcn). (**B**) Lifespan trajectories (*left* panel) and lifespan average effects (*right* panel) of Dex treatment on mtDNAcn expressed relative to the corresponding control time points for each donor. n = 3 donors per group, 5-8 timepoints per donor. Lifespan average graphs are mean ± SEM, two-way ANOVA. * $p < 0.05$, ns: not significant.

Extended Data Figure 4. Effects of chronic glucocorticoid signaling on mtDNAcn. (**A**) Correlation between cell-free mitochondrial DNA (cf-mtDNA) and cell-free nuclear DNA (cf-nDNA). (**B**) Lifespan trajectories (*left* panel) and lifespan average effects (*right* panel) of Dex treatment on cf-mtDNA/cf-nDNA ratio expressed relative to the corresponding control time points for each donor. (**C**) Correlation between cell-free (cf) and intracellular (int) mtDNA/nDNA ratio. (**D**) Lifespan average of cell-free (cf) and intracellular (int) mtDNA/nDNA ratio for under control conditions (*left* panel) and Dex treatment (*right* panel). n = 3 donors per group, 6-10 timepoints per donor. Lifespan average graphs are mean ± SEM, two-way ANOVA. Thick lines in correlation graphs show linear regression for each group, Pearson r correlation. * $p < 0.05$, ** $p < 0.01$, **** $p < 0.0001$, ns: not significant.

Extended Data Figure 5. Effects of chronic glucocorticoid signaling on gene expression of age-related cytokines. (**A**) Heatmaps showing the effect of Dex treatment on the expression of age-related cytokines, expressed as the Log_2 of fold change (Log_2FC) normalized gene expression relative to the corresponding control time points for each donor. (**B**) Lifespan trajectories of gene expression of each in cells treated with Dex relative to the corresponding control time points for each donor. Thin curves in soft red represents individual cytokines; thick curves in red represent the average of all cytokines evaluated; thick lines in gray represent the control level. (**C**) Lifespan trajectories (*left* panel) and average effects (*right* panel) of Dex treatment on *Stc1* gene (most upregulated gene) expression expressed relative to the corresponding control time point for each donor. (**D**) Same as C but for *Lum* gene (most downregulated gene). n = 3 donors per group, 9-10 timepoints per donor. Lifespan average graphs are mean ± SEM, two-way ANOVA. * $p < 0.05$, **** $p < 0.0001$, ns: not significant.

Extended Data Figure 6. Chronic glucocorticoid causes mtDNA instability. (**A**) Circos plots from mtDNA sequencing and Eclipse analysis for mtDNA. Red lines represent individual deletion break points that span the sequence contained between its two ends, and line darkness reflects the level of heteroplasmy for each deletion. The blue histograms represent coverage depth along the mtDNA sequence. (**B**) Lifespan trajectories (left panel) and lifespan average effects (right panel) of Dex treatment on the individual deletions count. (**C**) Frequency distribution of deletion lengths for all timepoints across lifespan. (**D**) Frequency of deletions (upper panels) and frequency of deletion break points (lower panels) along the mtDNA sequence. (**E**) Lifespan trajectories (left panel) and lifespan average effects (right panel) of Dex treatment on the deletions that span the D-loop region of the mtDNA. n = 3 donors per group, 2-6 timepoints per donor. Lifespan average graphs are mean ± SEM, two-way ANOVA. ns: not significant; N/A: not applicable.

Extended Data Figure 7. Effects of chronic glucocorticoid signaling on cell division. (**A**) Lifespan trajectories (*left* panel) and average effects (*right* panel) of Dex treatment on doubling rate (divisions/day) expressed relative to the corresponding control time points for each donor. (**B**) Same as A but for $J_{\text{ATP-Total}}$/cell volume/division. n = 3 donors per group, timepoints per donor: n = 26-36 in A, 8-13 in B. Lifespan average graphs are mean ± SEM, two-way ANOVA. **** $p < 0.0001$. ns: not significant. $J_{\text{ATP-Total}}$: algebraic sum of $J_{\text{ATP-Glyc}}$ and $J_{\text{ATPOxPhos}}$. $J_{\text{ATP-Glyc}}$: ATP production rate derived from glycolysis. $J_{\text{ATP-OxPhos}}$: ATP production rate derived from OxPhos.

Extended Data Figure 8. Effects of chronic glucocorticoid signaling on aging hallmarks. (**A**) Telomere length across population doublings calculated by the DNAmTL epigenetic clock with linear regressions for each donor of each group (**B**) Telomere length across population doublings calculated by the principal components (PC)-adjusted DNAmTL epigenetic clock with linear regressions for each donor of each group with linear regressions for each donor of each group (*left* panel), and telomere shortening rate calculated as the slope of the correspondent linear regressions (*right* panel). (**C**) Heatmaps showing the effect of Dex treatment on the expression of telomere maintenance-associated genes, expressed as the Log_2 fold change (Log_2FC) relative to the corresponding control time point for each donor. (**D**) Average effect of Dex treatment shown in C. Each datapoint represents the gene average of the Log_2FC values throughout the entire lifespan of the three donors. n = 3 donors per group, timepoints per donor: n = 4-13 in A-B, n = 9-10 in C. Thin lines in correlation graphs show linear regression for each donor, Pearson r correlation. Bar graphs are mean ± SEM, ratio paired t-test (two-tailed. * $p < 0.05$, ns: not significant.

Extended Data Figure 9. Effects of chronic glucocorticoid signaling on aging epigenetic clocks. (**A**) Epigenetic age across population doublings calculated by the DNAm Hannum epigenetic clock (*left* panel) and the principal components (PC)-adjusted version of it (*middle* panel), with linear regressions for each donor of each group, and the epigenetic aging rate calculated as the slope of the correspondent linear regressions (*right* panel). (**B-D**) Same as A but for Skin and Blood, Pan Tissue and Grimm Age epigenetic clocks, respectively. n = 3 donors per group, 4-13 timepoints per donor. Thin lines in correlation graphs show linear regression for each donor, Pearson r correlation. Bar graphs are mean ± SEM, ratio paired t-test (two-tailed). Ns: not significant.

Extended Data Figure 10. Hypermetabolism, not the metabolic shift towards OxPhos, predicts cell death. (**A**) Schematic of mitoNUITs mechanism of action, three pharmacological inhibitors of nutrient uptake in the mitochondria. (**B**) Lifespan average effects of Dex+mitoNUIT treatment on $J_{ATP\text{-}OxPhos}$/cell volume. (**C**) Same as (**B**) but for $J_{ATP\text{-}Glyc}$/cell volume. N = 3 donors per group, n=7-11 timepoints per donor. Lifespan average graphs are mean ± SEM, two-way ANOVA. * $p < 0.05$, ** $p < 0.01$, *** $p < 0.001$, **** $p < 0.0001$. mitoNUITs: Mitochondrial nutrient uptake inhibitors. $J_{ATP\text{-}Glyc}$: ATP production rate derived from glycolysis. $J_{ATP\text{-}OxPhos}$: ATP production rate derived from OxPhos

Supplemental Data Figure 1. Effects of chronic glucocorticoid signaling on gene expression. (A-E) Heatmaps from Figure 4 shown with complete labelling for gene-specific resolution. (**A**) Heatmaps showing the effect of Dex treatment on the expression of glycolytic genes, expressed as the Log_2 of fold change (Log_2FC) of normalized gene expression relative to the corresponding control time point for each donor. (**B**) Same as A but for genes that encodes for the subunits of Complex I, II, III, IV and V

(CI, CII, CIII, CIV, and CV) of OxPhos. (**C**) Same as A, but for genes associated with mtDNA replication. (**D**) Same as A but for genes associated with mtDNA maintenance. (**E**) Same as A but for genes associated with mitochondrial biogenesis. n = 3 donors per group, 9-10 timepoints per donor.

Supplemental Data Figure 2. Effects of chronic glucocorticoid signaling on secretion and gene expression of age-related cytokines. (**A-AB**) Lifespan trajectories (*left* panel) and average effects (*right* panel) of Dex treatment on age-related cytokines levels per mL of culture media (u*pper* panel) and normalized gene expression (*lower* panel), expressed relative to the corresponding control time point for each donor. n = 3 donors per group, 6-10 timepoints per donor. Lifespan average graphs are mean ± SEM, two-way ANOVA. * $p < 0.05$, ** $p < 0.01$, *** $p < 0.001$, **** $p < 0.0001$, ns: not significant

Figure 1

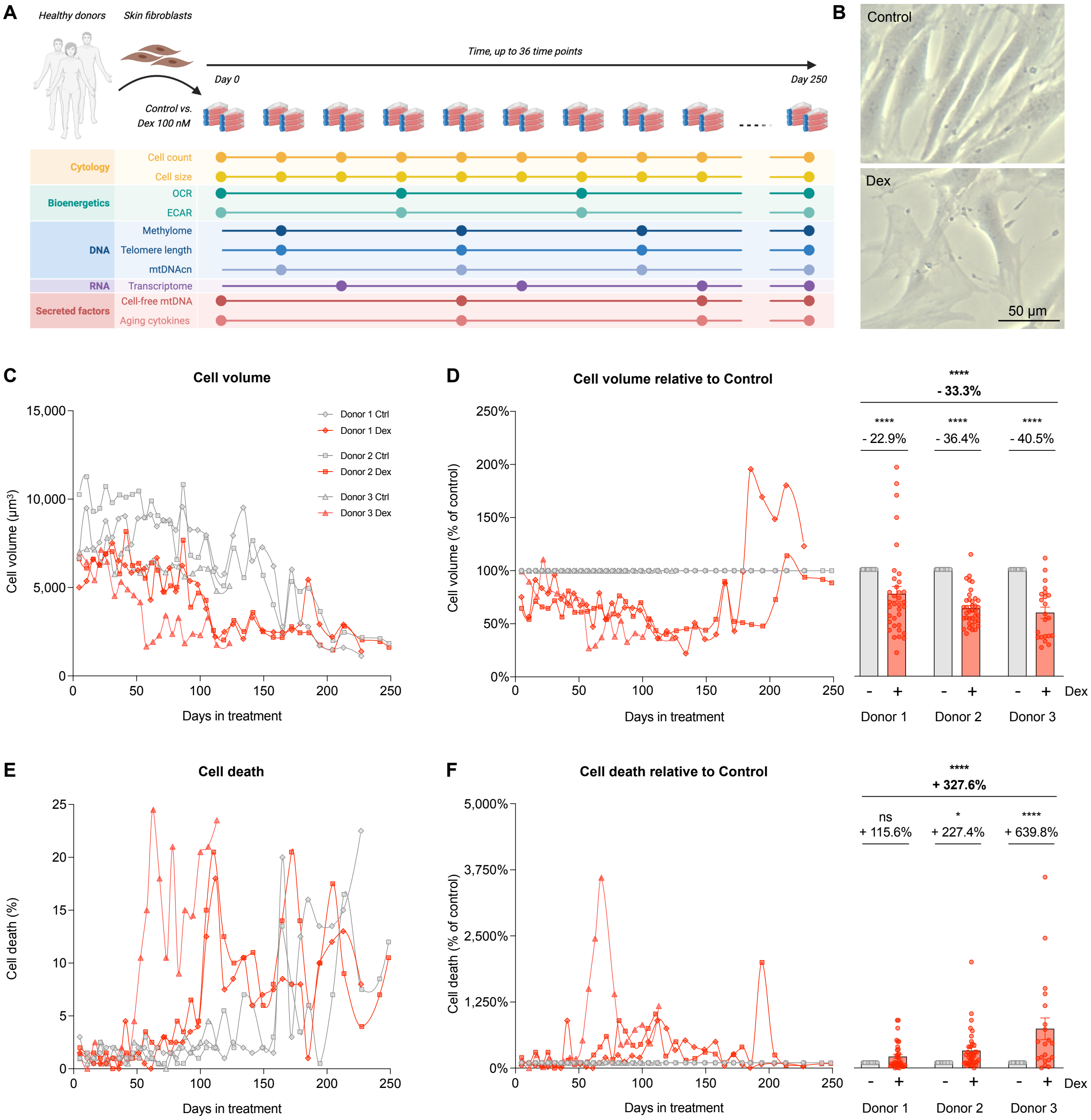
A
Healthy donors
Skin fibroblasts
Time, up to 36 time points
Day 0
Day 250
Control vs.
Dex 100 nM
Cytology
Cell count
Cell size
Bioenergetics
OCR
ECAR
DNA
Methylome
Telomere length
mtDNAcn
RNA
Transcriptome
Secreted factors
Cell-free mtDNA
Aging cytokines
B
Control
Dex
50 µm
C
Cell volume
Cell volume (µm³)
15,000
10,000
5,000
0
Days in treatment
0
50
100
150
200
250
Donor 1 Ctrl
Donor 1 Dex
Donor 2 Ctrl
Donor 2 Dex
Donor 3 Ctrl
Donor 3 Dex
D
Cell volume relative to Control
Cell volume (% of control)
250%
200%
150%
100%
50%
0%
Days in treatment
****
- 33.3%
****
- 22.9%
****
- 36.4%
****
- 40.5%
-
+
Dex
Donor 1
Donor 2
Donor 3
E
Cell death
Cell death (%)
25
20
15
10
5
0
Days in treatment
F
Cell death relative to Control
Cell death (% of control)
5,000%
3,750%
2,500%
1,250%
0%
Days in treatment
****
+ 327.6%
ns
+ 115.6%
*
+ 227.4%
****
+ 639.8%
Dex
Donor 1
Donor 2
Donor 3

Figure 2

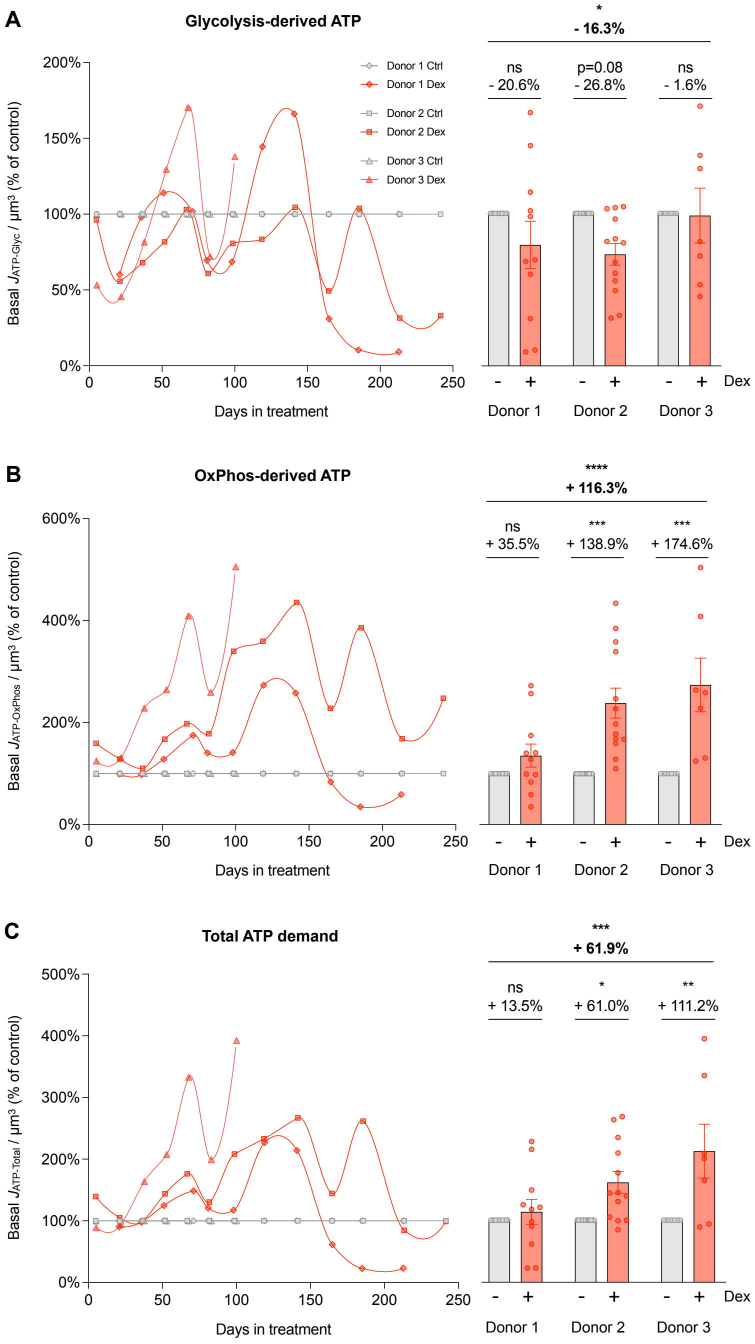
A
Glycolysis-derived ATP
Basal $J_{ATP-Glyc}$ / µm³ (% of control)
200%
150%
100%
50%
0%
0
50
100
150
200
250
Days in treatment
Donor 1 Ctrl
Donor 1 Dex
Donor 2 Ctrl
Donor 2 Dex
Donor 3 Ctrl
Donor 3 Dex
*
- 16.3%
ns
- 20.6%
p=0.08
- 26.8%
ns
- 1.6%
-
+
Dex
Donor 1
Donor 2
Donor 3
B
OxPhos-derived ATP
Basal $J_{ATP-OxPhos}$ / µm³ (% of control)
600%
400%
200%
0%
Days in treatment
****
+ 116.3%
ns
+ 35.5%
***
+ 138.9%
***
+ 174.6%
C
Total ATP demand
Basal $J_{ATP-Total}$ / µm³ (% of control)
500%
400%
300%
200%
100%
0%
Days in treatment
***
+ 61.9%
ns
+ 13.5%
*
+ 61.0%
**
+ 111.2%

Figure 3

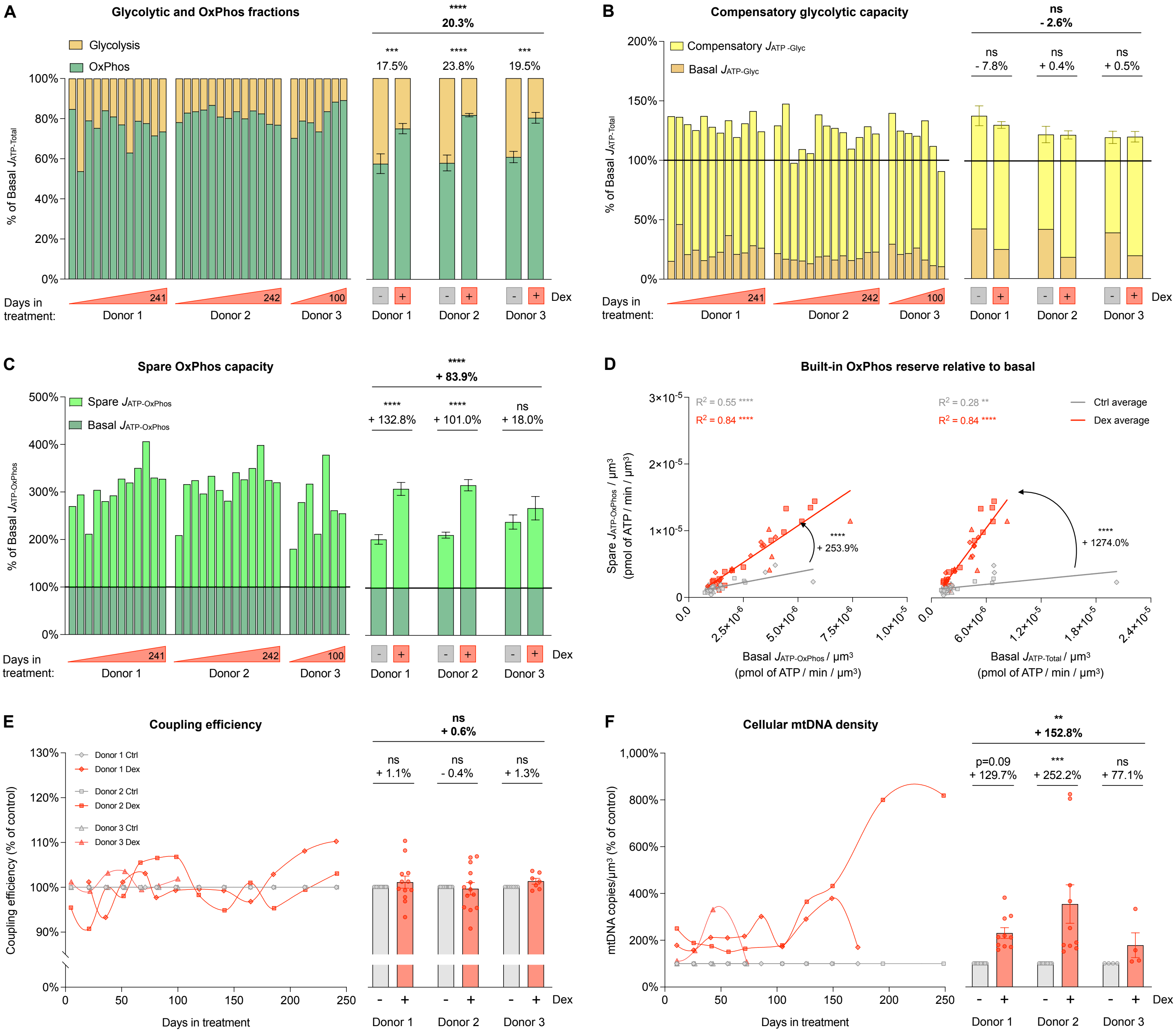
A
Glycolytic and OxPhos fractions
Glycolysis
OxPhos
% of Basal JATP-Total
100%
80%
60%
40%
20%
0%
Days in treatment:
241
242
100
Donor 1
Donor 2
Donor 3
****
20.3%
***
17.5%
****
23.8%
***
19.5%
-
+
Dex
B
Compensatory glycolytic capacity
Compensatory JATP -Glyc
Basal JATP-Glyc
% of Basal JATP-Total
200%
150%
100%
50%
0%
ns
- 2.6%
ns
- 7.8%
ns
+ 0.4%
ns
+ 0.5%
C
Spare OxPhos capacity
Spare JATP-OxPhos
Basal JATP-OxPhos
% of Basal JATP-OxPhos
500%
400%
300%
200%
100%
0%
****
+ 83.9%
****
+ 132.8%
****
+ 101.0%
ns
+ 18.0%
D
Built-in OxPhos reserve relative to basal
Spare JATP-OxPhos / µm3 (pmol of ATP / min / µm3)
3×10-5
2×10-5
1×10-5
0
R2 = 0.55 ****
R2 = 0.84 ****
R2 = 0.28 **
R2 = 0.84 ****
Ctrl average
Dex average
****
+ 253.9%
****
+ 1274.0%
0.0
2.5×10-6
5.0×10-6
7.5×10-6
1.0×10-5
Basal JATP-OxPhos / µm3 (pmol of ATP / min / µm3)
0.0
6.0×10-6
1.2×10-5
1.8×10-5
2.4×10-5
Basal JATP-Total / µm3 (pmol of ATP / min / µm3)
E
Coupling efficiency
Coupling efficiency (% of control)
130%
120%
110%
100%
90%
0%
Donor 1 Ctrl
Donor 1 Dex
Donor 2 Ctrl
Donor 2 Dex
Donor 3 Ctrl
Donor 3 Dex
0
50
100
150
200
250
Days in treatment
ns
+ 0.6%
ns
+ 1.1%
ns
- 0.4%
ns
+ 1.3%
F
Cellular mtDNA density
mtDNA copies/µm3 (% of control)
1,000%
800%
600%
400%
200%
0%
**
+ 152.8%
p=0.09
+ 129.7%
***
+ 252.2%
ns
+ 77.1%

Figure 4

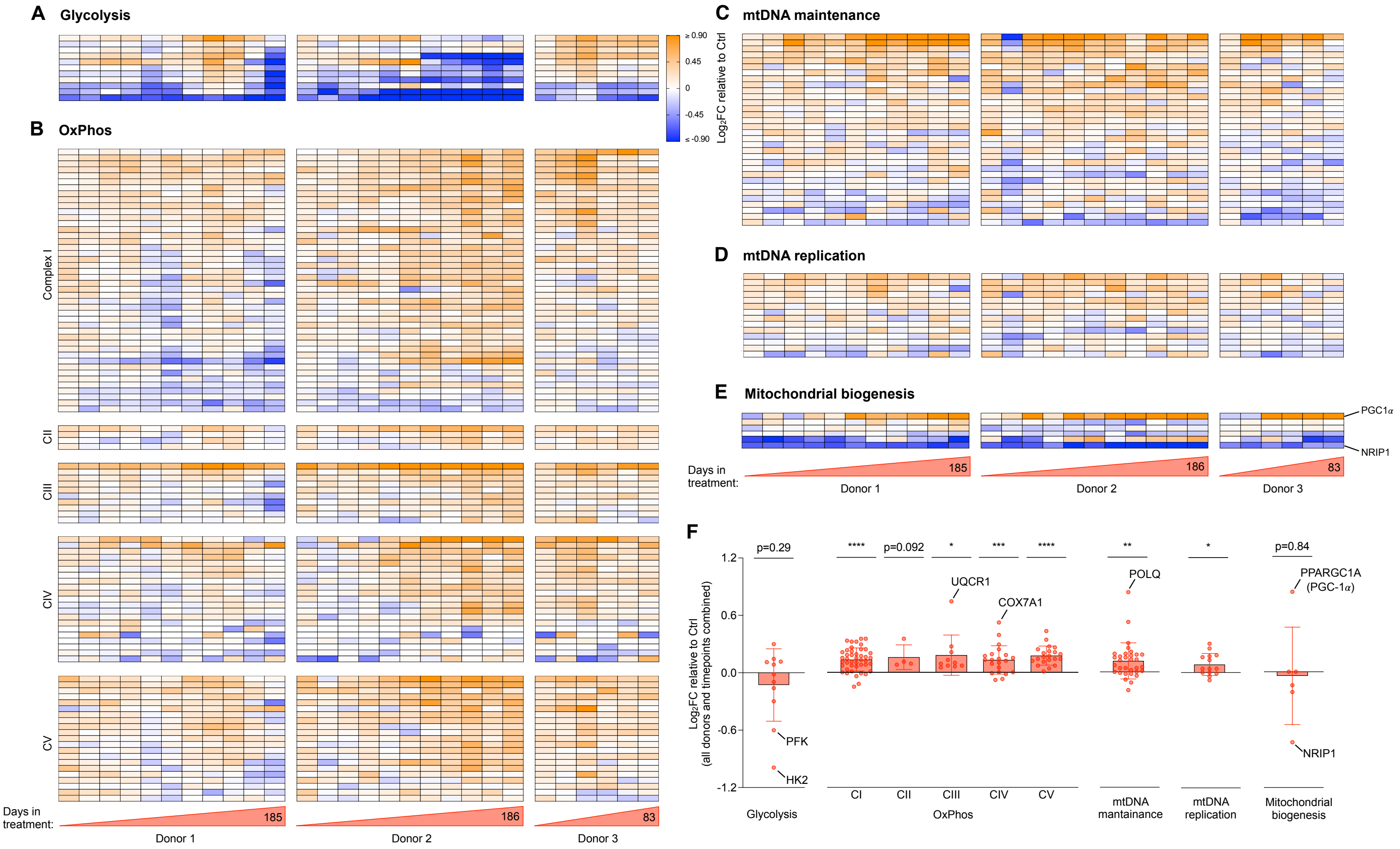
A Glycolysis
B OxPhos
Complex I
CII
CIII
CIV
CV
≥ 0.90
0.45
0
-0.45
≤ -0.90
Log2FC relative to Ctrl
C mtDNA maintenance
D mtDNA replication
E Mitochondrial biogenesis
PGC1α
NRIP1
Days in treatment:
185
186
83
Donor 1
Donor 2
Donor 3
F
Log2FC relative to Ctrl (all donors and timepoints combined)
1.2
0.6
0.0
-0.6
-1.2
p=0.29
****
p=0.092
*
***
****
**
*
p=0.84
UQCR1
COX7A1
POLQ
PPARGC1A (PGC-1α)
PFK
HK2
NRIP1
CI
CII
CIII
CIV
CV
Glycolysis
OxPhos
mtDNA mantainance
mtDNA replication
Mitochondrial biogenesis

Figure 5

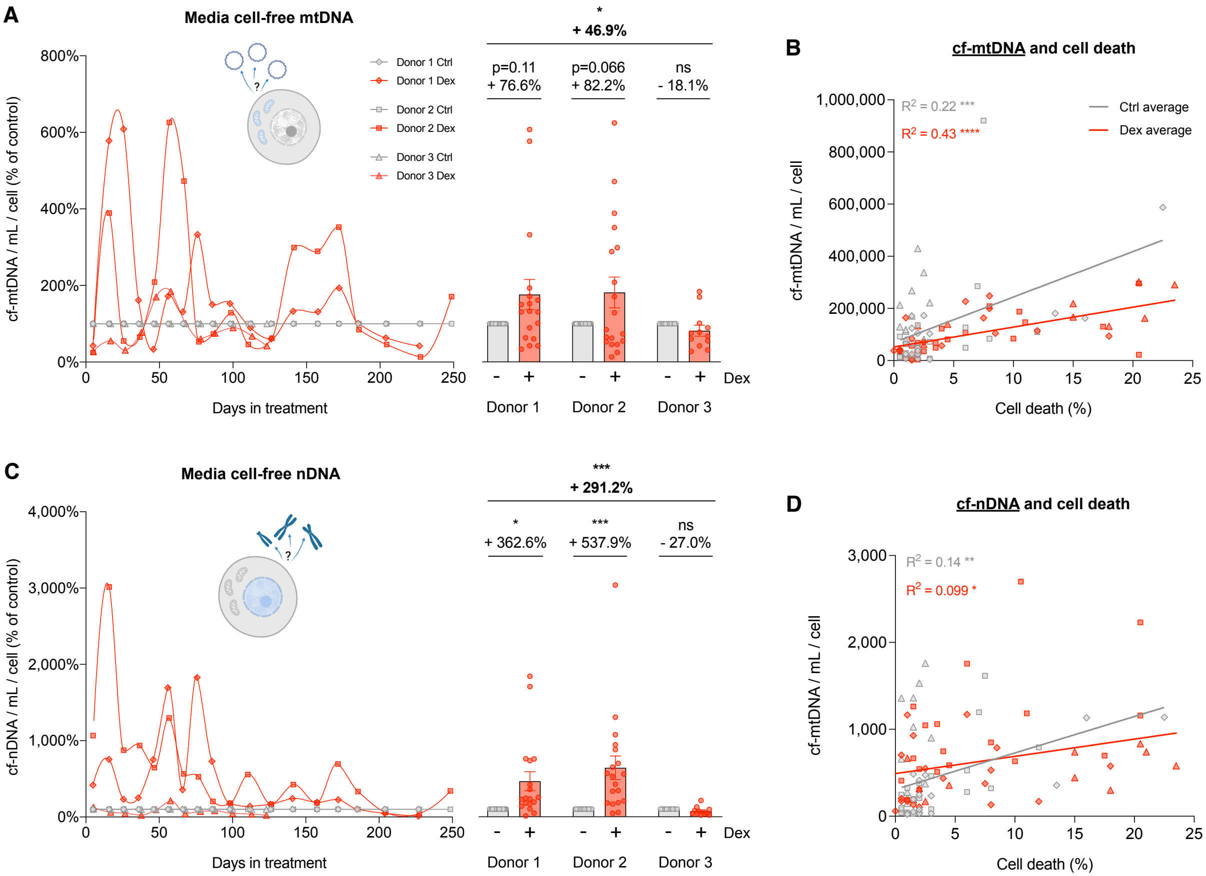
A
Media cell-free mtDNA
cf-mtDNA / mL / cell (% of control)
800%
600%
400%
200%
0%
0
50
100
150
200
250
Days in treatment
Donor 1 Ctrl
Donor 1 Dex
Donor 2 Ctrl
Donor 2 Dex
Donor 3 Ctrl
Donor 3 Dex
?
*
+ 46.9%
p=0.11
+ 76.6%
p=0.066
+ 82.2%
ns
- 18.1%
-
+
Dex
Donor 1
Donor 2
Donor 3
B
cf-mtDNA and cell death
cf-mtDNA / mL / cell
1,000,000
800,000
600,000
400,000
200,000
0
R^2 = 0.22 ***
R^2 = 0.43 ****
Ctrl average
Dex average
0
5
10
15
20
25
Cell death (%)
C
Media cell-free nDNA
cf-nDNA / mL / cell (% of control)
4,000%
3,000%
2,000%
1,000%
0%
0
50
100
150
200
250
Days in treatment
?
***
+ 291.2%
*
+ 362.6%
***
+ 537.9%
ns
- 27.0%
-
+
Dex
Donor 1
Donor 2
Donor 3
D
cf-nDNA and cell death
cf-mtDNA / mL / cell
3,000
2,000
1,000
0
R^2 = 0.14 **
R^2 = 0.099 *
0
5
10
15
20
25
Cell death (%)

Figure 6

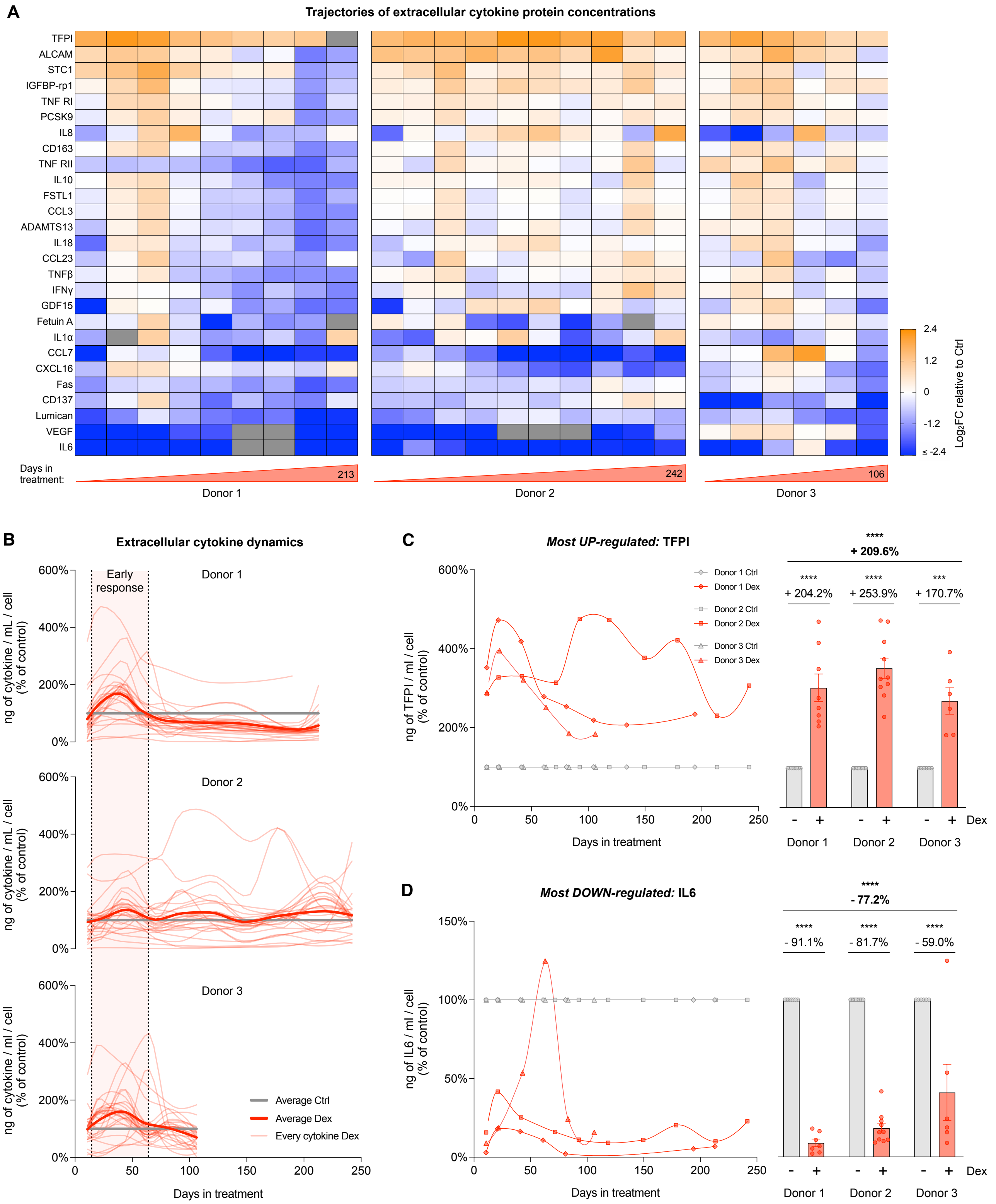
A
Trajectories of extracellular cytokine protein concentrations
TFPI
ALCAM
STC1
IGFBP-rp1
TNF RI
PCSK9
IL8
CD163
TNF RII
IL10
FSTL1
CCL3
ADAMTS13
IL18
CCL23
TNFβ
IFNγ
GDF15
Fetuin A
IL1α
CCL7
CXCL16
Fas
CD137
Lumican
VEGF
IL6
2.4
1.2
0
-1.2
≤ -2.4
Log₂FC relative to Ctrl
Days in treatment:
213
242
106
Donor 1
Donor 2
Donor 3
B
Extracellular cytokine dynamics
Early response
Donor 1
Donor 2
Donor 3
600%
400%
200%
0%
ng of cytokine / mL / cell (% of control)
ng of cytokine / ml / cell (% of control)
Average Ctrl
Average Dex
Every cytokine Dex
0
50
100
150
200
250
Days in treatment
C
Most UP-regulated: TFPI
ng of TFPI / ml / cell (% of control)
Donor 1 Ctrl
Donor 1 Dex
Donor 2 Ctrl
Donor 2 Dex
Donor 3 Ctrl
Donor 3 Dex
****
+ 209.6%
****
+ 204.2%
****
+ 253.9%
***
+ 170.7%
- + - + - + Dex
Donor 1
Donor 2
Donor 3
D
Most DOWN-regulated: IL6
ng of IL6 / ml / cell (% of control)
150%
100%
50%
0%
****
- 77.2%
****
- 91.1%
****
- 81.7%
****
- 59.0%
Days in treatment

Figure 7

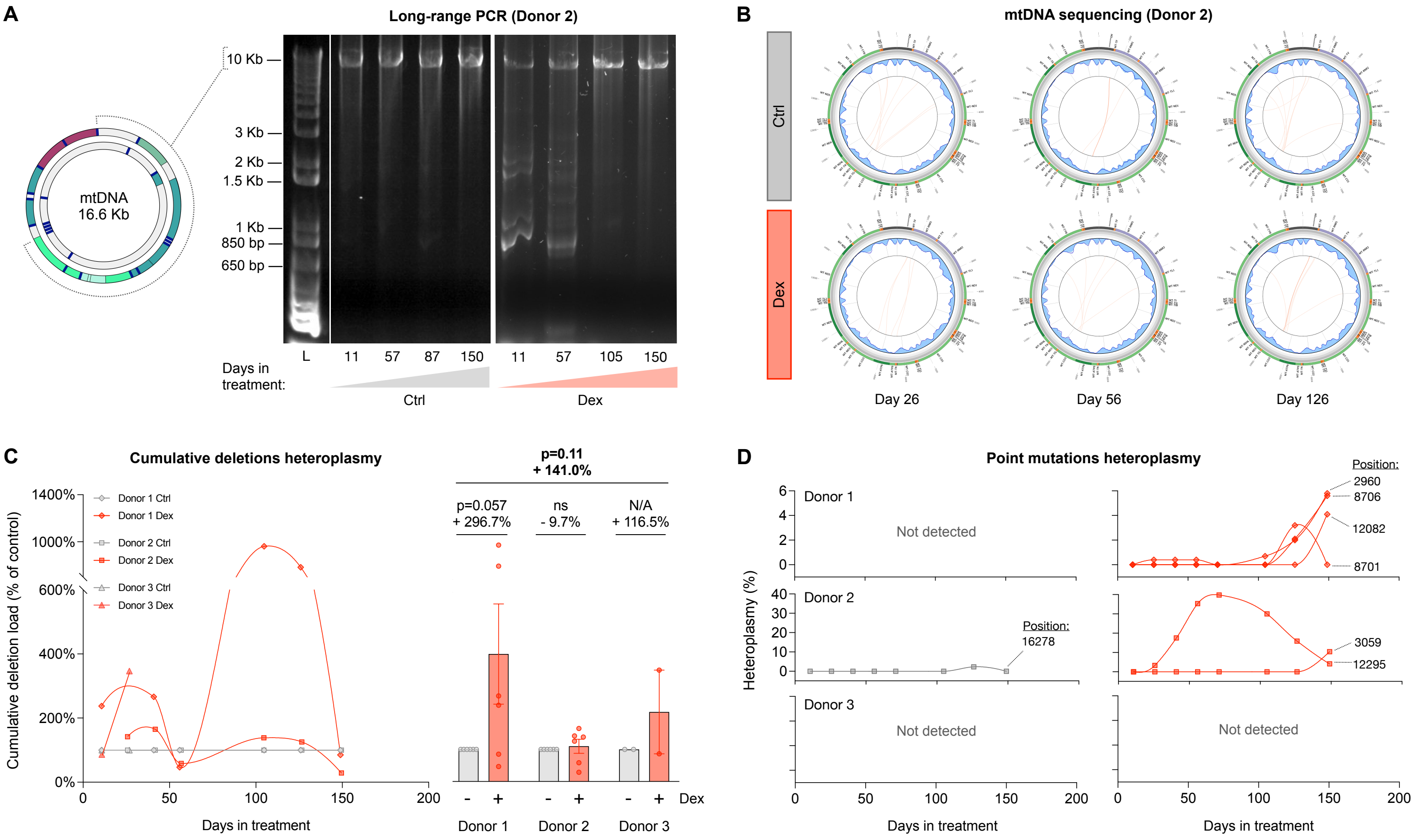
A
Long-range PCR (Donor 2)
mtDNA
16.6 Kb
10 Kb
3 Kb
2 Kb
1.5 Kb
1 Kb
850 bp
650 bp
L
11
57
87
150
11
57
105
150
Days in treatment:
Ctrl
Dex
B
mtDNA sequencing (Donor 2)
Ctrl
Dex
Day 26
Day 56
Day 126
C
Cumulative deletions heteroplasmy
Cumulative deletion load (% of control)
1400%
1000%
600%
400%
200%
0%
Donor 1 Ctrl
Donor 1 Dex
Donor 2 Ctrl
Donor 2 Dex
Donor 3 Ctrl
Donor 3 Dex
0
50
100
150
200
Days in treatment
p=0.11
+ 141.0%
p=0.057
+ 296.7%
ns
- 9.7%
N/A
+ 116.5%
-
+
Dex
Donor 1
Donor 2
Donor 3
D
Point mutations heteroplasmy
Heteroplasmy (%)
Donor 1
Not detected
6
4
2
0
Position:
2960
8706
12082
8701
Donor 2
40
30
20
10
0
Position:
16278
3059
12295
Donor 3
Not detected
Not detected
0
50
100
150
200
Days in treatment

Figure 8

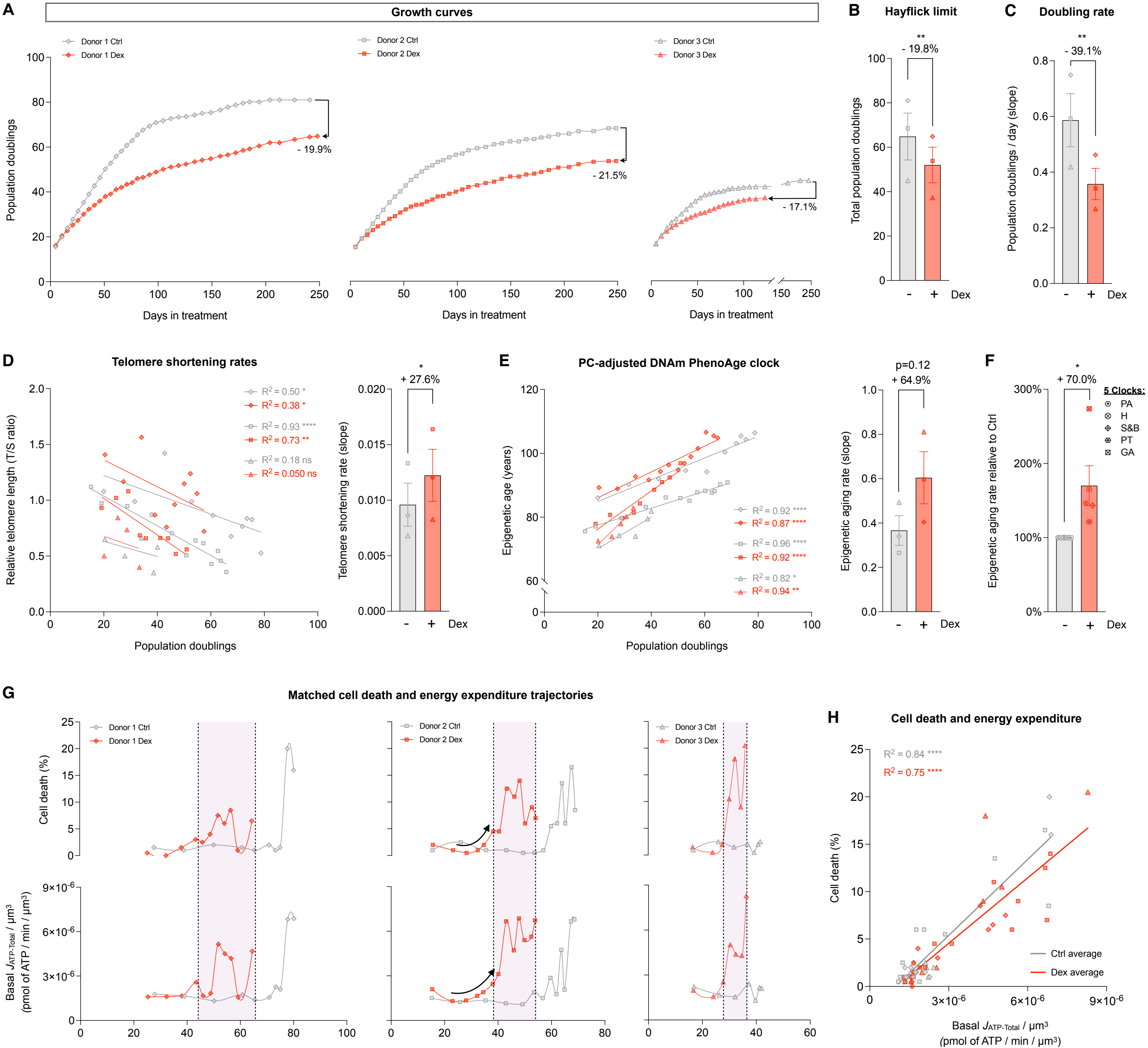
A
Growth curves
Donor 1 Ctrl
Donor 1 Dex
Donor 2 Ctrl
Donor 2 Dex
Donor 3 Ctrl
Donor 3 Dex
Population doublings
Days in treatment
- 19.9%
- 21.5%
- 17.1%
B
Hayflick limit
Total population doublings
**
- 19.8%
Dex
C
Doubling rate
Population doublings / day (slope)
**
- 39.1%
D
Telomere shortening rates
Relative telomere length (T/S ratio)
R² = 0.50 *
R² = 0.38 *
R² = 0.93 ****
R² = 0.73 **
R² = 0.18 ns
R² = 0.050 ns
Population doublings
Telomere shortening rate (slope)
*
+ 27.6%
E
PC-adjusted DNAm PhenoAge clock
Epigenetic age (years)
R² = 0.92 ****
R² = 0.87 ****
R² = 0.96 ****
R² = 0.92 ****
R² = 0.82 *
R² = 0.94 **
Epigenetic aging rate (slope)
p=0.12
+ 64.9%
F
Epigenetic aging rate relative to Ctrl
*
+ 70.0%
5 Clocks:
PA
H
S&B
PT
GA
G
Matched cell death and energy expenditure trajectories
Cell death (%)
Basal J_ATP-Total / µm³ (pmol of ATP / min / µm³)
Population doublings
H
Cell death and energy expenditure
R² = 0.84 ****
R² = 0.75 ****
Ctrl average
Dex average
Cell death (%)
Basal J_ATP-Total / µm³ (pmol of ATP / min / µm³)

Figure 9

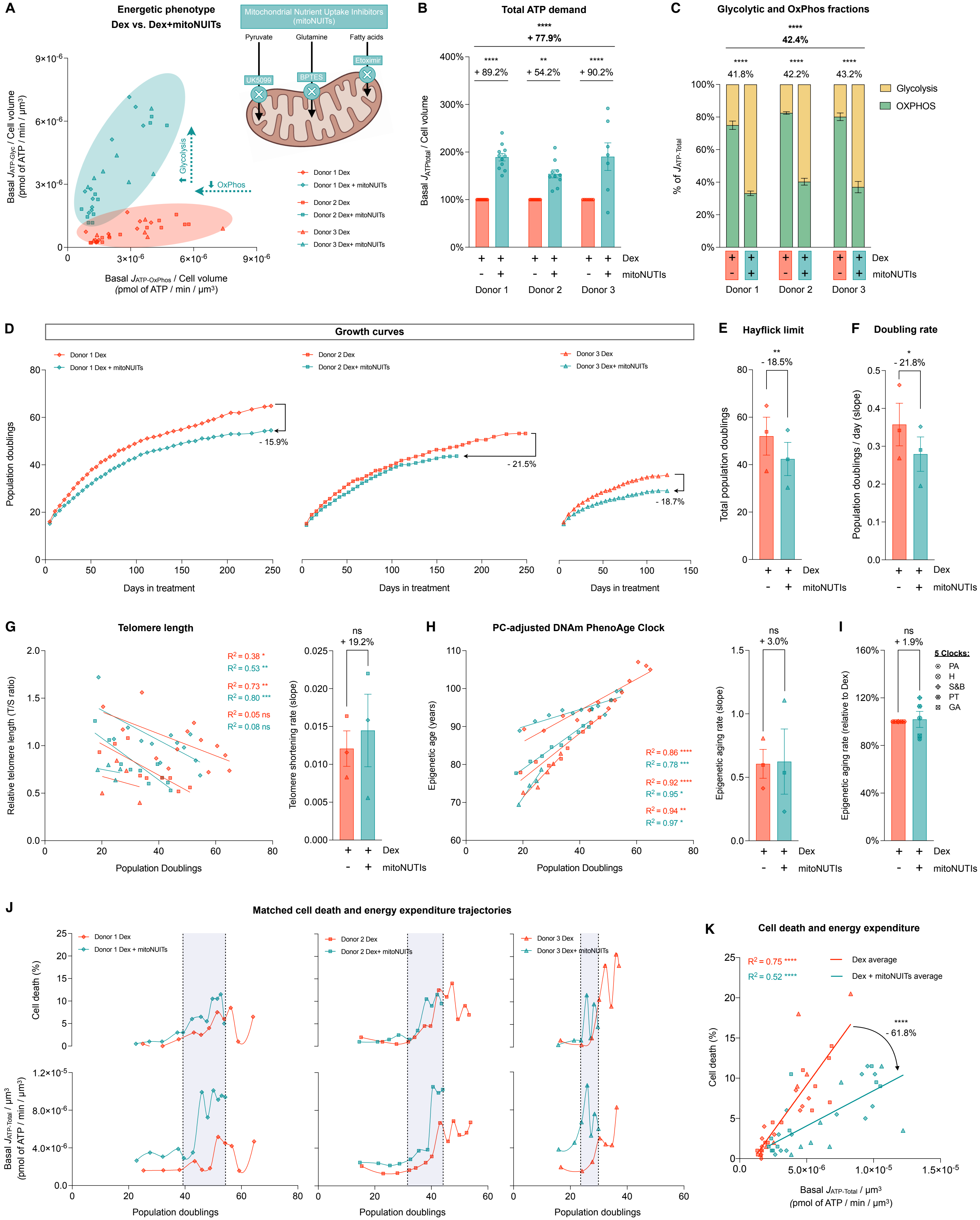
A
Energetic phenotype
Dex vs. Dex+mitoNUITs
Mitochondrial Nutrient Uptake Inhibitors (mitoNUITs)
Pyruvate
Glutamine
Fatty acids
UK5099
BPTES
Etoximir
Glycolysis
OxPhos
Basal $J_{ATP-Glyc}$ / Cell volume (pmol of ATP / min / µm³)
Basal $J_{ATP-OxPhos}$ / Cell volume (pmol of ATP / min / µm³)
Donor 1 Dex
Donor 1 Dex + mitoNUITs
Donor 2 Dex
Donor 2 Dex+ mitoNUITs
Donor 3 Dex
Donor 3 Dex+ mitoNUITs
B
Total ATP demand
**** + 77.9%
**** + 89.2%
** + 54.2%
**** + 90.2%
Basal $J_{ATPtotal}$ / Cell volume
Dex
mitoNUITs
Donor 1
Donor 2
Donor 3
C
Glycolytic and OxPhos fractions
**** 42.4%
**** 41.8%
**** 42.2%
**** 43.2%
% of $J_{ATP-Total}$
Glycolysis
OXPHOS
D
Growth curves
Population doublings
Days in treatment
- 15.9%
- 21.5%
- 18.7%
E
Hayflick limit
** - 18.5%
Total population doublings
F
Doubling rate
* - 21.8%
Population doublings / day (slope)
G
Telomere length
Relative telomere length (T/S ratio)
Population Doublings
R^2 = 0.38 *
R^2 = 0.53 **
R^2 = 0.73 **
R^2 = 0.80 ***
R^2 = 0.05 ns
R^2 = 0.08 ns
ns + 19.2%
Telomere shortening rate (slope)
H
PC-adjusted DNAm PhenoAge Clock
Epigenetic age (years)
R^2 = 0.86 ****
R^2 = 0.78 ***
R^2 = 0.92 ****
R^2 = 0.95 *
R^2 = 0.94 **
R^2 = 0.97 *
ns + 3.0%
Epigenetic aging rate (slope)
I
ns + 1.9%
Epigenetic aging rate (relative to Dex)
5 Clocks:
PA
H
S&B
PT
GA
J
Matched cell death and energy expenditure trajectories
Cell death (%)
Basal $J_{ATP-Total}$ / µm³ (pmol of ATP / min / µm³)
Population doublings
K
Cell death and energy expenditure
R^2 = 0.75 ****
R^2 = 0.52 ****
Dex average
Dex + mitoNUITs average
**** - 61.8%
Cell death (%)
Basal $J_{ATP-Total}$ / µm³ (pmol of ATP / min / µm³)

Figure 10

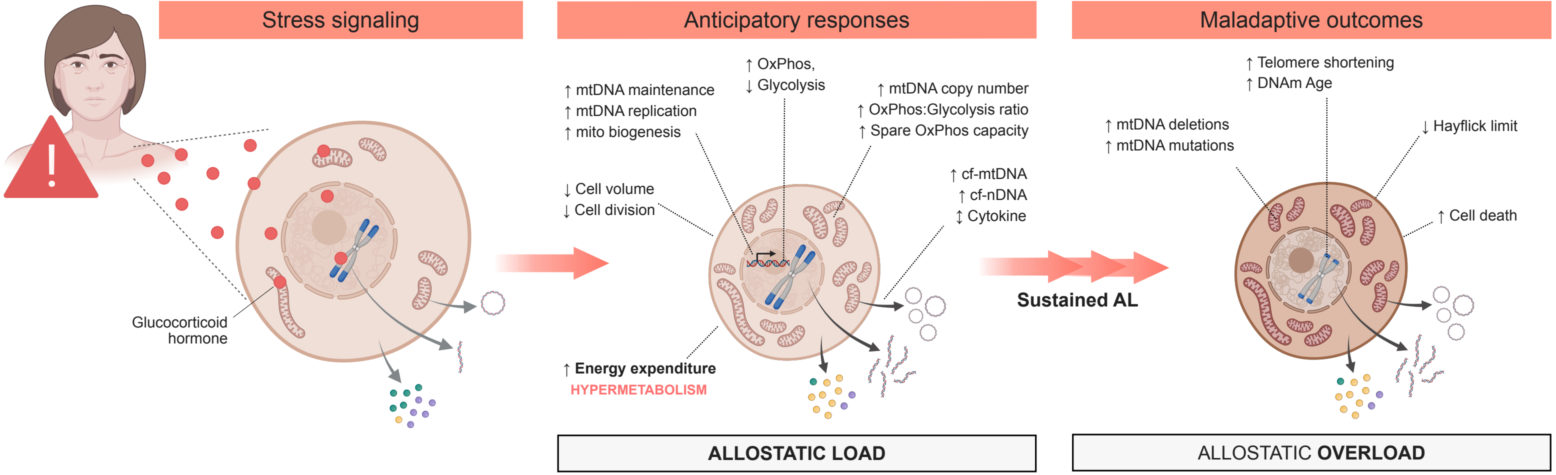
Stress signaling
Anticipatory responses
Maladaptive outcomes
Glucocorticoid hormone
↑ mtDNA maintenance
↑ mtDNA replication
↑ mito biogenesis
↑ OxPhos,
↓ Glycolysis
↑ mtDNA copy number
↑ OxPhos:Glycolysis ratio
↑ Spare OxPhos capacity
↓ Cell volume
↓ Cell division
↑ cf-mtDNA
↑ cf-nDNA
↕ Cytokine
↑ Energy expenditure
HYPERMETABOLISM
Sustained AL
↑ Telomere shortening
↑ DNAm Age
↑ mtDNA deletions
↑ mtDNA mutations
↓ Hayflick limit
↑ Cell death
ALLOSTATIC LOAD
ALLOSTATIC OVERLOAD